Exploration of a Future NOAA Infrared Sounder in Geostationary Earth Orbit

Flavio Iturbide-Sanchez, *Senior Member, IEEE*, Zhipeng Wang, Satya Kalluri, Yong Chen, Erin Lynch, Murty Divakarla, Changyi Tan, Tong Zhu, and Changyong Cao

***Abstract*—A geostationary (GEO) hyperspectral infrared sounder (HyIRS) is capable of providing high spectral (0.625 cm^{-1}), temporal (every 30 min) and spatial (4 km) resolution observations over the continental U.S. (CONUS). Frequent observations from a GEO-HyIRS at high spatial resolution are expected to contribute to the generation of three-dimensional structures of atmospheric temperature and humidity, and wind. These new observations will provide valuable information for timely forecasts of severe storms over the CONUS and the overall Western Hemisphere. Infrared (IR) sounder observations from a geostationary orbit open a new set of possibilities, including the capability of monitoring the diurnal cycle of atmospheric patterns, which is difficult from Low Earth Orbit IR sounders and the capability of timely and accurate retrievals of several trace gases. In this article, the feasibility of adding a HyIRS into the next generation of U.S. geostationary environmental satellites is studied. The configuration of a notional U.S. GEO-HyIRS sensor and its ground data processing system are discussed. A hyperspectral IR data simulator is developed and reported as part of this engineering study, where proxy data is used to model the end-to-end ground processing system. Various considerations for the configuration and the calibration and validation of the instrument are addressed.**

***Index Terms*—Calibration, geostationary, infrared, remote sensing, sounder.**

I. Introduction

HYPERSPECTRAL infrared sounders (HyIRS) are key remote sensing instruments used to construct vertical profiles of atmospheric temperature and moisture for meteorological and climatological research. HyIRS is a type of meteorological sensor that can be deployed in LEO or GEO orbit. Radiances from HyIRS sensors on Sun synchronous polar orbiting satellites are routinely assimilated into Numerical Weather Prediction (NWP) models, which has been shown to improve forecast skill. This type of meteorological sensors, along with microwave sensors, has been very cost-effective and shown significant positive impact on global NWP applications. Examples of such instruments are the National Aeronautics and Space Administration (NASA) Atmospheric Infrared Sounder (AIRS) [1], the European Organization for the Exploitation of Meteorological Satellites (EUMETSAT) Infrared Atmospheric Sounding Interferometer (IASI) [2], and the Joint Polar Satellite System (JPSS) Cross-track Infrared Sounder (CrIS) [3]. The HyIRS sensors are capable of sensing changes in thermodynamic variables (temperature and water vapor), trace gas species (carbon dioxide, methane, carbon monoxide, ozone, among others) as well as critical climate variables such as surface temperature.

A HyIRS in a Geostationary (GEO-HyIRS) orbit can provide Earth observations with improved spatial and temporal resolution compared to LEO IR sounders, and thus, provide highly valuable information to improve the understanding of the entire life cycle of convective systems and the forecasting of severe weather events [4], [5]. Several Observing System Simulation Experiments (OSSEs) have demonstrated the benefits of observations from a GEO-HyIRS. In [6], data assimilation experiments demonstrate the improvement in the forecast of representative meteorological fields, including moisture, temperature, wind, heavy rainfall, as well as reduction in the tropical cyclone track forecast errors associated with the assimilation of frequent clear-sky radiances from a GEO-HyIRS. A previous study, reported in [7], shows the benefits of assimilating high spatial and temporal resolution GEO-HyIRS observations in short-term forecasting of severe storms. The OSSE results presented in [8] indicate the potential improvement in the specific humidity modelling from the assimilation of observations from the geostationary EUMETSAT Meteosat Third Generation Sounding Satellite (MTG-S) Infrared Sounder (IRS).

Several meteorological and space agencies have either launched or plan to launch HyIRS sounders in GEO orbit. The China Meteorological Administration (CMA) launched the Geostationary Interferometric Infrared Sounder (GIIRS) on board the FY-4A on May 1, 2018. The value of these new type of high temporal observations to improve the quality of atmospheric

Manuscript received August 26, 2021; revised November 3, 2021 and December 12, 2021; accepted December 29, 2021. Date of publication January 11, 2022; date of current version February 9, 2022. This work was supported by the NOAA/NESDIS/Office of Projects, Planning, and Analysis under the Technology Maturation Program. *(Corresponding author: Flavio Iturbide-Sanchez.)*

Flavio Iturbide-Sanchez, Yong Chen, and Changyong Cao are with the NOAA/NESDIS/Center for Satellite Applications and Research, College Park, MD 20740 USA (e-mail: flavio.iturbide@noaa.gov; yong.chen@noaa.gov; changyong.cao@noaa.gov).

Zhipeng Wang is with the Science Systems and Applications Inc., Greenbelt, MD 20706 USA (e-mail: zhipeng.wang@noaa.gov).

Satya Kalluri is with the NOAA/NESDIS/Joint Polar Satellite System Program Office, Greenbelt, MD 20771 USA (e-mail: satya.kalluri@noaa.gov).

Erin Lynch is with the NOAA/NESDIS/Office of Projects, Planning, and Analysis, Silver Spring, MD 20910 USA (e-mail: erin.lynch@noaa.gov).

Murty Divakarla, Changyi Tan, and Tong Zhu are with the I. M. Systems Group, Inc., Rockville, MD 20852 USA (e-mail: murty.divakarla@noaa.gov; changyi.tan@noaa.gov; tong.zhu@noaa.gov).

Digital Object Identifier 10.1109/JSTARS.2022.3142069

wind profiles and the forecast of track and intensity of tropical cyclones has been recently demonstrated [9]–[13]. EUMETSAT is planning to launch the IRS onboard the MTG-S satellite towards the end of 2023 [14]–[18]. The Japan Meteorological Agency (JMA) is planning to include a HyIRS instrument as part of the discussions of the follow-on program for the operational geostationary satellites Himawari-8 and -9, which are scheduled to operate around 2029 [6]. In the same direction, the National Oceanic and Atmospheric Administration (NOAA) National Environmental Satellite, Data, and Information Service (NESDIS) has conducted preformulation studies to perform technical and cost assessments for including a HyIRS sensor in the NOAA's Geostationary Extended Observations (GeoXO) satellite system, as a successor of the Geostationary Operational Environmental Satellites (GOES) sounder [19], [20]. As part of the recommended GeoXO constellation, a GEO centrally-located spacecraft will carry a hyperspectral infrared Sounder (GXS) with the objective to provide real-time information of thermodynamic vertical profiles for numerical weather prediction and nowcasting [21]. The GXS is expected to complement the present efforts made by Europe and Asia, and to advance the response to the vision for space in 2040 of the World Meteorological Organization (WMO) Integrated Global Observing System [22], [23].

The purpose of this engineering study is to model the data characteristics and ground data processing requirements for a GEO-HyIRS sensor, using the NOAA CrIS sensor as a proxy. The study is aligned with the NOAA/NESDIS strategic goal to provide observational leadership in geostationary observations in a timely manner to both promote and protect the Nation's environment, security, economy, and quality of life. This article was supported by the NOAA/NESDIS/Office of Projects, Planning, and Analysis under the Technology Maturation Program.

This article starts with a summary of benefits of an operational GEO-HyIRS and the analysis of LEO/GEO-HyIRS sensors that are currently operated by international agencies, and those that are planned for future launches by partner agencies (see Section II). Section III discusses the configuration of a notional GEO-HyIRS instrument that holds specific spectral, spatial, and temporal characteristics, while Section IV is dedicated to discuss the hypothetical configuration of the ground segment (GS) for the GEO-HyIRS instrument. A software simulator was developed to produce GEO HyIRS proxy data using Suomi National Polar-orbiting Partnership (S-NPP) and NOAA-20 CrIS observations. This data helped to enable the design and testing of an end-to-end data processing system on the ground. The simulation results are provided in Section V. Various considerations and challenges for the calibration and validation of a GEO-HyIRS are discussed in Section VI, along with several subtopics on data simulation, allocation of calibration and validation modules. This section also includes the benefits of applying principal component compression (PCC) to the GEO-HyIRS observations. Concluding remarks and a summary of this article are given in Section VII.

II. GEO-HyIRS Background

A. Benefits of an Operational GEO-HyIRS

The accuracy of NWP depends on the quality of observations from a variety of sources, a high-performance computer system, and an advanced numerical model with data assimilation technology [24]. Satellite-based remote sensing instruments can acquire information about the structure of geophysical variables at a global scale, which are critical input to the global/regional NWP models. While an infrared imager can provide a comprehensive horizontal representation of the atmosphere, only an IR sounder can provide information about the three-dimensional (3-D) structure of atmospheric variables, including temperature, humidity, and wind. This capability enables the possibility of tracking the evolution of atmospheric variables, particularly if observations are made frequently. For example, performing observations from geostationary sounders allows the monitoring of the diurnal cycle of atmospheric patterns.

A major drawback of the legacy infrared sounders, such as the GOES-N, O, P series, is that their spectral bands are too broad to resolve the individual atmospheric absorption lines and can only yield coarse vertical resolution, thus limiting the ability to observe the atmosphere's structures. For example, the old-generation GOES sounders only have 18 IR bands at a resolution of 10–100 cm^{-1} for a single band. Instead, present HyIRS instruments are able to provide measurements at very fine spectral resolution on the order of 0.5 cm^{-1}. This enables measurements of important changes in the vertical structure of the atmosphere at a resolution of 1-2 km, depending on altitude [25]. A hyperspectral sounder can also support the monitoring and forecasting of air quality by providing estimates of diurnal variations of atmospheric trace gases like ozone and carbon monoxide. This capability has been demonstrated by existing LEO IR sounders, such as AIRS, IASI, and CrIS [26]–[28]. While a LEO-sounder can provide global atmospheric profile data, one satellite can only cover any given location of the earth twice per day (except for the polar regions). Even worse, the location of a storm development may coincide with the orbital gaps of a LEO satellite, causing a disruption in the continuity of the monitoring of the weather event. As a result, existing LEO-sounders are only suitable for the coverage of large-scale weather systems, such as those falling within the synoptic scale.

GEO satellite systems circulate the earth at an altitude of about 36 000 km above the equator with an orbital period of 24 h. Therefore, they are stationary above a certain point above the equator. An advanced sounding mission from geostationary orbit can provide the high spectral, high temporal, and high spatial resolution observations needed for the timely forecasting of severe thunderstorms and tropical cyclones. This accounts for the assimilation of these type of observations into NWP forecast models that impact 12-72-h forecasts and beyond [29], and short-term forecasts that predict the weather within approximately a 6-h window (nowcasting). Presently, the value of assimilating observations from LEO hyperspectral infrared sensors into regional models is limited by the poor latency associated with observations from LEO sensors [30]. However, the

TABLE I
KEY PARAMETERS OF CURRENT AND PLANNED HYPERSPECTRAL IR SOUNDERS IN GEOSTATIONARY ORBIT COMPARED TO THE LEO CRIS

Sensor	GIIRS [9-13]	MTG-IRS [14-18]	GIFTS [25]	CrIS[5] [3]
Country	China	Europe	U.S.	U.S.
Satellite	FY-4	MTG-S	EO-3 (Canceled)	S-NPP/NOAA-20
Launch Date	2016	2024	Cancelled in 2006	2011/2017
Design Lifetime (year)	7	16 (mission)	N/A	7
Instrument Type	Interferometer	Interferometer	Interferometer	Interferometer
Spectral Bands (No. Channels)	LWIR:700 -1130 cm^{-1} (689) MWIR: 1650 -2250 cm^{-1} (961)	LWIR:700-1210 cm^{-1} (>800) MWIR: 1600-2175 cm^{-1} (>920)	LWIR: 685-1130 cm^{-1} MWIR: 1470-2275 cm^{-1}	LWIR: 650-1095 cm^{-1} (713) MWIR: 1210-1750 cm^{-1} (865) SWIR: 2155-2550 cm^{-1} (633)
Spatial Resolution (km)	16	4	4	14
Number of Detectors (per band)	32×4	160×160	128×128	3×3
Spectral Resolution (Sampling) (cm^{-1})	0.625	<0.754 (0.625)	0.6-38.4	(0.625)
Spectral Accuracy (ppm)	10	5-10[1]	10	10
Radiometric Accuracy (K)	1.5	0.5	1	0.45/0.58/0.77
Noise (mW/(m2·sr·cm^{-1}))	LWIR:0.5-1.1, MWIR:0.1-0.14	0.1-0.2 K	<0.4/<0.06 (objective)	0.14/0.084/0.014
Coverage	MESO/China	Europe/FD	MESO/US/FD	Global
Repeat Cycle	<30 min / <1 h	30 min / 6 h	-	12 h
Dwelling Time (s)	21	10	10	0.2 (per Field of Regard)
Downlink Rate (Mbps)	-	167[2]	135[3]	2.5[4]

[1]The published requirement is 0.1 K equivalent, corresponding to a band dependent spectral accuracy of about 5–10 ppm.
[2]Data Compression information is not available.
[3]Data Rate before compression.
[4]Date Rate after compression.
[5]CrIS is a LEO sensor. It is listed as a main proxy sensor for this study. The spectral information is for CrIS operating in full spectral resolution mode.

benefits of LEO HyIRS observations to support nowcasting have been demonstrated. This is the case of a recent study that shows that operational JPSS CrIS observations can be used to support the analysis of preconvective environments [31]. In this regard, more frequent observations of thermodynamic atmospheric profiles from an operational GEO-HyIRS are expected to result in enhanced nowcasting capabilities. Moreover, GEO-HyIRS sensors are being planned with higher spatial resolution than present IR sounders in LEO orbit, which is expected to further benefit nowcasting and NWP applications due to the increased probability of finding clear-sky conditions [32].

Because a GEO-HyIRS observes the earth at high altitude, smaller earth view scan angles of less than 7.5° for all scenes are possible, making the shapes of the field-of-views (FOVs) among detectors far more uniform than those found in the LEO sensor observations, where the typical earth view scan angles are within a range of $\pm 45°$. This particular characteristic of geostationary sensor observations makes the interpretation of the observed radiance simpler. On the other hand, the maximum viewing angle at the earth surface, or local viewing zenith angle, for a GEO-HyIRS can be as large as 90° at the peripheral region of the full disk (FD) of the earth. Thus, the temperature gradients in the slant path could not be neglected in the simulations of the observed radiances by current fast radiative transfer models (for example, most fast radiative transfer models can not handle local zenith angle greater than 65°). Due to that, either the selected scenes should be restricted to those associated with smaller viewing angles, or the impact of the slant path should be considered in the radiance simulation process [33].

The capability of generating accurate retrievals of several trace gases, such as H_2O, CO_2, and O_3, can also be enhanced with a GEO IR sounder due to its superior spatial and temporal resolving power. For example, the diurnal variation of these trace gases can be routinely monitored over a regional domain. Moreover, the value of geostationary IR sounders is not limited to the nowcasting of severe weather; its benefits extend to other applications, including monitoring atmospheric composition (due to its diurnal cycle capabilities), volcanic activity, fires, and other extreme events.

B. Heritage LEO and GEO-HyIRS

Several major meteorological and space agencies either have launched or plan to launch hyperspectral sounders into geostationary orbits, such as the GIIRS aboard the CMA FY-4 and the IRS aboard the EUMETSAT MTG-S satellite. Table I compares the technical capabilities and key parameters of these sounders, as well as the NOAA CrIS sensor in LEO orbit, which is used as a main proxy IR sounder to design many of the instrument parameters presented in this engineering study. The list also includes the Geostationary Imaging Fourier Transform Spectrometer (GIFTS) for the cancelled NASA EO-3 mission. As observed from Table I, the value of the hyperspectral IR sounders on geostationary orbit resides on their capability to provide observations with repeated cycles of about 30 min, spatial resolution of up to 4 km, radiometric accuracy better than 1.5 K, and spectral accuracy better than 10 parts per million (ppm), along with high radiometric sensitivity associated with their low radiometric noise. In terms of spectral coverage, the IR sounders basically cover the long-wave infrared (LWIR), the mid-wave infrared (MWIR), and the short-wave infrared (SWIR) spectral ranges, which hold critical information for the sensing of atmospheric temperature, tropospheric water vapor as well as trace gases. In terms of instrument design, the infrared sensors listed in Table I are Fourier transform spectrometers (FTS). Due to the high spatial, temporal, and spectral resolution,

high downlink data rates over 100 Mb/s are required for the GEO infrared sounders. For example, the LEO CrIS sensor has on-board data processing similar to the MTG-IRS, but it only requires a downlink data rate of about 2.5 Mb/s.

C. Technical Parameters of a GEO-HyIRS for NWP Applications

To provide valuable data for NWP and nowcasting applications, the GEO-HyIRS should meet strict requirements for spectral, spatial and temporal coverage. The GEO-HyIRS shall cover a Contiguous U.S. (CONUS) scene at least every 30 min (compared to 5 min for the NOAA's GOES R-series (GOES-R) Advanced Baseline Imager (ABI)) and cover a FD Western Hemisphere scene every 60 min (10 min for ABI).

Based on the instrument parameters reported in Table I, these requirements could be met using a dwell consisting of about 155 $\times$ 155 FOVs at 4 km resolution at nadir (or 112 μrad in ground sample angle) measured approximately every 10 s. For a GEO sensor to cover a FD image, its field-of-regard (FOR), which corresponds to the total area observable by the sensor, needs to be at least 17.5°. The actual FOR needs to be large enough to allow for the observations of both the earth disk and the deep space at the earth limb for detector background subtraction, along with other imposed margins. A FOR value of 20° should be adequate for the GEO-HyIRS. At the same time, a maximum local view zenith angle of about 60° is recommended to reduce slant path effects [33]. The dwelling observation time of each FOV is determined to be 10 s (similar to the EUMETSAT MTG-IRS). Radiometric and spectral requirements are set similar to CrIS. These technical parameter requirements are consistent with the planned GXS [34]. In this article, a downlink data rate close to 90 Mb/s was used as a design requirement, since this is close to the actual data rate used in the configuration of the operational GOES-R ABI instrument and its ground data processing system [35], [36]. This design requirement is in line with the GIFTS and MTG-IRS specifications and with the instrument science and engineering data rate requirement, of less than 150 Mb/s, of the GXS sensor [34].

III. Configuration of a GEO-HyIRS Instrument

The hypothetical instrument configuration and the scanning scheme of the notional GEO-HyIRS was defined after establishing a tradeoff between data volume, temporal coverage, and spatial resolution. The strategy used to define the configuration and design parameters of the GEO-HyIRS instrument was to perform a tradeoff analysis using the instrument downlink data rate as an anchor parameter. The downlink data rate is one of the major limiting and critical instrument design parameters since it influences not only the instrument characteristics, but also the design and cost of the ground segment system. In order to determine the GEO-HyIRS data rate, the CrIS downlink data rate was used as a reference and was scaled to define key parameters of the GEO-HyIRS instrument, such as spatial resolution, spectral coverage, dwell observation period, and the number of detectors per dwell. By using the CrIS as reference, it is assumed that the GEO-HyIRS will be an FTS spectrometer,

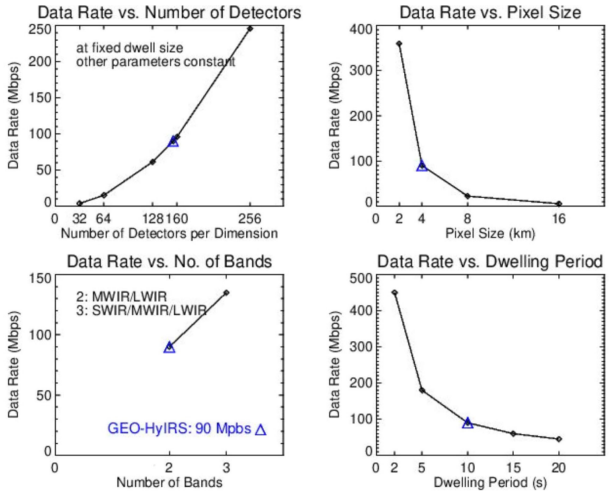

Fig. 1. Dependency of RDR data volume/rate as a function of focal plane array size (Top-left), spatial resolution (Top-right), number of spectral bands (Bottom-left) and dwelling period (Bottom-right). The blue diamond indicates the GEO-HyIRS configuration that would provide a downlink data rate of 90 Mb/s.

having similar on-board data processing to CrIS. This is a valid assumption, since planned GEO-HyIRS instruments like the MTG-IRS or GIFTS, are also FTS spectrometers with on-board data processing equivalent to CrIS.

The advantage of using CrIS as a reference is that it is an operational sensor that meets the NWP requirements with a robust design and GS architecture that has provided science data since 2012. The CrIS data rate is approximately 2.5 Mb/s and includes compressed complex interferograms, telemetry as well as calibration parameters and tables in the form of raw data record (RDR) packets. In this analysis, 910 samples per interferogram per spectral band and an average of 10.5 bits per interferogram sample were assumed. These parameter values are very close to the values found in the CrIS sensor. This information along with the dwelling period and size, FOV spatial resolution and the number of spectral bands was used to determine the GEO-HyIRS RDR data rate (see Fig. 1). With respect to the spectral bands, the notional GEO-HyIRS is expected to have LWIR and MWIR bands with the spectral coverage defined in Table II. Results presented in Fig. 1 clearly illustrate how fast the downlink data rate increases as the number of detectors and spatial resolution increase or as the dwelling period decreases.

In this article, the GOES was used as a reference for the GS architecture of the GEO-HyIRS. In Fig. 1, the blue triangle indicates the GEO-HyIRS configuration that would provide a downlink data rate of 90 Mb/s. Based on this baseline requirement and assuming: 1) a dwelling observation time of 10 s and a spatial resolution of 4 km, which are compatible with the GIFTS and MTG-IRS specifications, and 2) the selection of two spectral bands (LWIR/MWIR), the notional GEO-HyIRS instrument configuration is reported in Table II. Table II shows that the required focal plane array size consists of 155$\times$155 detectors. This implies that each instrument dwell observation has the capability to cover about 620$\times$620 km^2 every 10 s. The size of the focal plane array is very consistent with the

TABLE II
POTENTIAL CONFIGURATION OF THE NOTIONAL NOAA GEOSTATIONARY HYPERSPECTRAL INFRARED SOUNDER COMPARED TO THE EUMETSAT MTG-IRS INSTRUMENT CONFIGURATION

Sensors	MTG-IRS	GEO-HyIRS
Satellite Platform	MTG-S	GeoXO
Spatial Resolution (km)	4	4
Detector Assembly (per band)	160×160	155×155[1]
Dwelling Period (s)	10	10
Spectral Range (cm^{-1})	LWIR:700-1210 MWIR: 1600-2175	LWIR: 680-1095 MWIR: 1689-2250
Instrument Type	Interferometer	Interferometer
SDR Data Precision (bit)	16	16
Scan Mode (region)	Europe / FD	CONUS / FD
Number of Dwells	70 / 280	35 / 292
Region Data Processing Latency (min)	Not Available	<10 / <30
Scan Repeat Cycle	30 min / 6 h	30 min / 1 h
Field-of-Regard (°)	17.5	20
Spectral Sampling (cm^{-1})	0.625	0.625
ICT Calibration Interval (min)	15	5
RDR Downlink Rate (Mbps)	~167[2]	90[3]
RDR Data Volume (GB/day)	Not Available	961

[1]Detector assembly size is derived from a trade-off between Coverage Rate and Downlink Data Volume.
[2]https://earth.esa.int/web/eoportal/satellite-missions/m/meteosat-third-generation.
[3]The data are compressed with CrIS approach before downlink.

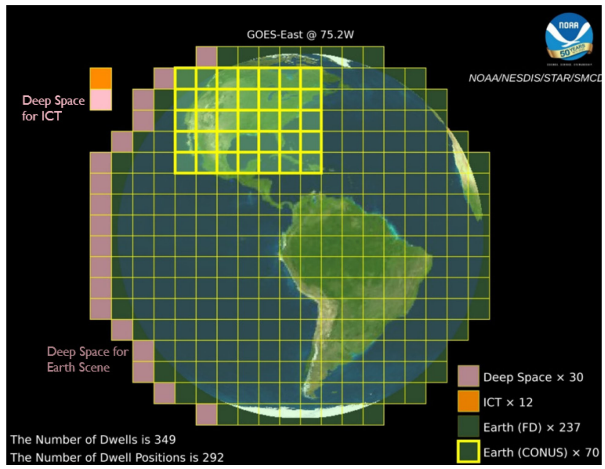

Fig. 2. Notional 60-min scanning scheme of the GEO HyIRS instrument, designed to cover the CONUS scene every 30 min and the FD scene every 60 min. A total of 349 dwells have been identified: CONUS scene has $35\times2=70$ (35 dwell positions and each dwell position is scanned twice) dwells in total, the ICT scene has 12 dwells, the DS scene has 30 dwells and the FD scene (excluding CONUS) has 237 dwells.

TABLE III
GOE-HYIRS SCAN TIMELINE SUMMARY

Scene Type	# OF DWELL POSITIONS (N)	Repeats in a Timeline (p)	# of Dwell Images (N×p)	Duration (min:s)
CONUS	35	2	70	11:40
FD (no CONUS)	237	1	237	39:30
ICT	1	12	12	2:00
Deep Space Type I	1	12	12	2:00
Deep Space Type II	18	1	18	3:00
Total	292	-	349	58:10*

*The remaining time of the 1-h timeline is reserved for scan mirror movement, telemetry collection, etc.

MTG-IRS. The data volume of RDR and calibrated observations in the form of Sensor Data Record (SDR) per day is expected to be close to 1 TB. For the calculation of the SDR data volume, the CrIS SDRs at full spectral resolution (FSR) were used as proxy data. The CrIS SDRs account for geolocation information.

In order to provide valuable data for NWP and nowcasting applications, it was established that the GEO-HyIRS should cover a CONUS scene every 30 min and cover a FD Western Hemisphere scene every 60 min. In terms of data processing latency, less than 10 min should be recommended for the CONUS region and less than 30 min for the FD. The notional scanning configuration of the GEO-HyIRS that repeats approximately every 60 min is illustrated in Fig. 2. It includes: 1) earth scene (ES) dwell observations as well as 2) Internal Calibration Target (ICT) or hot temperature reference dwell observations, and 3) deep space (DS) or cold temperature reference dwell observations, required for sensor calibration. The notional scanning sequence could consist of, first, performing 35 consecutive ES dwell observations over the CONUS region (identified by area with yellow-color dwells) within an estimated time of 5 m:50 s. Then, the FD is partially covered with approximately 118 consecutive ES dwell observations (illustrated by green-color dwells) within about 19 m:40 s. This sequence is repeated twice to cover the FD and the CONUS twice within less than 60 min. In this configuration, ICT dwell observations are performed approximately every 5 min to calibrate the instrument against instrument gain or temperature change variations. For the GEO-HyIRS, two types of DS observations have been considered. One type provides the background signal for the ICT observations, at the limb of the earth when each E-W scan starts. The time intervals between the DS observations are thus varying with the numbers of dwells in the row from 90 s to 190 s. The other type of DS observations is for the actual calibration of the ES observations. This type of DS observations is made with the same frequency as the ICT calibration. The viewing directions of the two types of DS views are, thus, different.

In total, 349 dwell observations will be collected within about 1 h: 70 (35×2) ES dwells over the CONUS region, 237 ES dwell observations outside the CONUS region as well as 12 ICT dwells and 30 DS dwells for sensor calibration. The scan timeline of the GEO-HyIRS is summarized in Table III. It is important to highlight that all the parameters and configurations assumed in this analysis can be scaled accordingly.

The main purpose of the performed analysis was to establish a baseline configuration for the GEO-HyIRS sounder, with the objective of performing the corresponding feasibility study to identify major challenges in terms of instrument design and calibration as well as GS architecture design and cost.

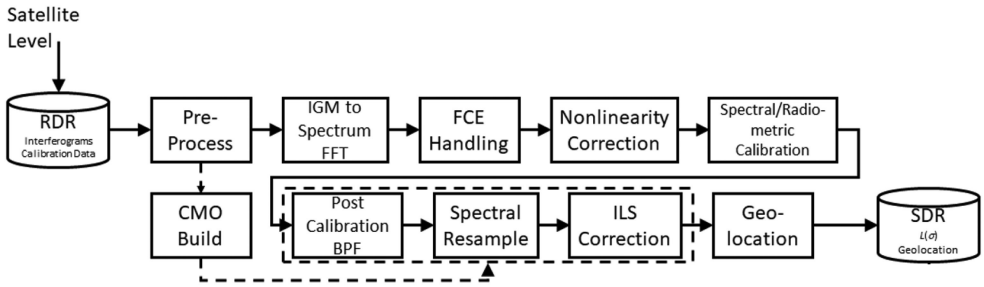

Fig. 3. Ground data processing system of the GEO-HyIRS (based on the operational CrIS sensor ground data processing architecture).

IV. Configuration of the Ground Segment System for the GEO-HyIRS Instrument

For the GEO-HyIRS, the configuration of the GS is a critical component of the whole system and needs to be considered in this engineering study. Similar to the current GOES satellites, the GEO-HyIRS GS architecture is assumed to operate from three sites and two Operations Support Locations. The NOAA Satellite Operations Facility in Suitland, MD houses the primary Mission Management (MM) functions of Tracking, Telemetry and Command, the Product Generation (PG) functions of Level 2+ (L2+) product generation, and the Product Distribution (PD) of Level 2+ products. The Wallops Command and Data Acquisition Station in Wallops Island, VA provides space communications services and Level 1B (L1B) product generation. The third site is a geographically isolated Consolidated Backup Facility (CBU) located at Fairmont, West Virginia. The CBU functions as a completely independent backup for designated MM, PG, and PD functions for the production and delivery of L1B data. The L1B sensor radiances from the hyperspectral sounder will be the Key Performance Parameters for the mission as they are expected to be assimilated in NWP models. In this hypothetical setup, the CBU has visibility to all operational and on-orbit spare satellites. The L2+ products are expected to be retrievals of atmospheric temperature, water vapor, trace gasses and winds, along with derived atmospheric stability parameters that go to the NOAA National Weather Service forecasters at the Weather Forecast Offices.

An important element of this article was to determine the data rates from the sensor so that the ground segment system can be adequately sized. The notional instrument would have a fairly high data rate, combining high sounder imaging cadence ($<$ 60 min FD refresh) with moderately high spatial resolution (in the 3–5 km nadir range). Spectrally, the GXS instrument is expected to have a similar resolution to that of the JPSS CrIS sensor [34], providing a good tradeoff between signal to noise ratio performance and vertical resolution. In this engineering study, we analyzed the design and specifications of hyperspectral sounders in a geostationary orbit that are currently operating and those that are planned to be launched. This includes the CMA GIIRS sensor, which was launched in 2016 aboard the FY-4A satellite, and the EUMETSAT IRS sounder, aboard the MTG-S satellite.

A. Main Modules for the GEO-HyIRS L1B Generation

The purpose of the GS data processing system is to convert the downlinked interferograms into radiometrically, spectrally, and geometrically calibrated radiance spectra, also known as L1B data or SDR products. We expect to follow the data processing flow of the CrIS instrument, which has been operational since 2012. The main functional modules of the GEO-HyIRS ground segment system are illustrated in Fig. 3. This system is expected to have similar architecture to the operational CrIS ground segment system. The main data processing modules are briefly described below. Further details can be found in the CrIS SDR Algorithm Theoretical Basis Document [37].

1) *The preprocessing module:* The data input to the GS processing system are science RDR or Level-0 (L0) data, which is composed of raw Consultative Committee for Space Data Systems packets from the spacecraft, together with added metadata such as spacecraft level ephemeris and attitude information. The preprocessing module unpacks the L0 data and application packets, sorts the interferograms based on time, FOV and FOR, performs quality control tests, and establishes the calibration 4-min moving window for averaging DS and ICT data. The module also computes the laser metrology wavelength from neon calibration data for the spectral calibration.
2) *Fast fourier transform module:* This module converts the ES, DS, and ICT interferograms to raw spectra. The raw spectra are wider than the spectra of the final L1B data, and the extra spectral bins at the beginning and end of the L1B spectra (guard band) are discarded at the end of the L1B data processing.
3) *Fringe count error handling module:* The module detects and corrects phase errors of the raw spectra due to interferogram sampling shifts.
4) *Nonlinearity correction module*: This module removes the second-order nonlinearity by scaling the raw spectrum with a factor applied for all channels within a spectral band (LWIR/MWIR/SWIR). The instrument nonlinearity arises mainly from the detectors as well as the signal conditioning electronics.
5) *Radiometric calibration module:* The instrument detectors and electronics are designed to yield, in principle, an output that is linear with respect to the incident radiance. The two-point radiometric calibration is performed on the

ES spectrum using the DS and ICT spectra as calibration references to determine the slope and offset of the linear relationship. The module also detects events where the Moon enters into the DS view (lunar radiation intrusion) and removes its contamination from the calculation of the background signal [38]. The ES spectra calibrated during a lunar intrusion event are marked with the lunar intrusion flag to indicate lunar intrusion occurrence. The module also computes the noise equivalent differential radiance (NEdN) for each ES spectrum, derived from ICT spectra observations.

6) The next three operational modules, enclosed in the dashed box of Fig. 3, are needed to perform the spectral correction [39], [40].
   i) *Digital band-pass filter (BPF) module:* The BPF is applied to attenuate the noise signal in the guard bands, which were amplified during the radiometric calibration. This operation prevents the guard band noise from leaking into the in-band signal of the two subsequent spectral correction operations.
   ii) *Spectral resample module:* This module maps the spectrum from the instrument's spectral grid, determined by laser metrology wavelength and the radiometric maximum path difference, onto a defined common user's spectral grid.
   iii) *Instrument line shape function correction module:* The module removes the interferometer's self-apodization effect from spectra. As a result, the spectral response function associated with the L1B spectrum is close to an ideal Sinc function. This module helps to make the calibrated spectra less FOV dependent, which is highly important for NWP applications.
7) *Geolocation module:* The geolocation module computes the GEO-HyIRS line-of-sight (LOS) pointing vector relative to the spacecraft body frame for each FOV and scan position. The LOS vector is then passed to the spacecraft level geolocation algorithms to compute the FOV center location including the geodetic longitude and latitude. Similar to the ABI L1B data, spatial resampling is expected to be applied to the GEO-HyIRS observations in order to project them onto fixed grid angular coordinates [36]. As part of this article, spatial resampling was applied during the generation of the GEO-HyIRS proxy data, described in Section V-A. However, the spatial resampling was not accounted for in the configuration of the ground data processing system reported in Section IV-B.

The final L1B data product includes complex ES radiance spectra, ICT radiance noise in the form of NEdN, geolocation data, and various quality control (QC) and quality assurance (QA) variables and flags, such as the SDR overall quality flag. The calibrated observations are distributed to NWP users and used to produce EDR (L2+) products for downstream users. Some of the ground segment processing modules could potentially be shifted to the on-board processing, following similar approaches found for the IASI instrument [2].

TABLE IV
ESTIMATED TIME TO PROCESS ONE GEO-HYIRS DWELL WITH 1-CPU

	Case 1	Case 2	Case 3	Case 4	Case 5	Case 6	Case 7	Case 8	Case 9	Case 10	Case 11	Case 12
CPU1	547s	559s	548s	545s	545s	545s	548s	550s	543s	535s	555s	599s
CPU2	550s	559s	547s	547s	547s	549s	545s	552s	543s	536s	554s	603s
CPU3	557s	606s	593s	594s	593s	594s	592s	598s	585s	580s	609s	652s
CPU4	549s	562s	549s	546s	548s	548s	549s	552s	542s	536s	553s	600s
Average	551s	572s	559s	558s	558s	559s	559s	563s	553s	547s	568s	614s
	559s (averaged with the first 11 cases)						569s (averaged with all cases)					

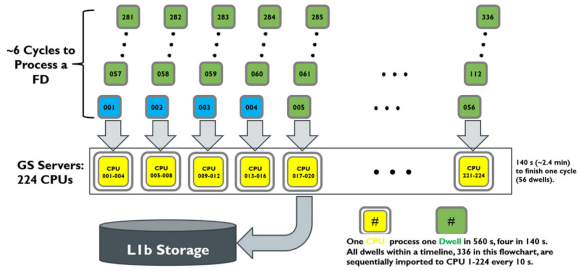

Fig. 4. Data processing configuration for the ground segment system of the notional GEO-HyIRS. The configuration aims to process a FD using approximately six data processing cycles. During each data processing cycle a total of 56 dwells are processed simultaneously.

B. GEO-HyIRS L1B Data Processing Configuration

As part of this project, the data processing configuration for the ground segment system of the notional GEO-HyIRS was defined. For this purpose, the following assumptions were made as follows.

1) One GEO-HyIRS dwell corresponds to 155 × 155 FOVs = 24025 FOVs.
2) The GEO-HyIRS covers two bands, resulting in 24025 × 2 = 48050 interferograms.
3) The number of data points per interferogram was assumed to be the same as for the CrIS system, which corresponds to approximately 1000 data points per interferogram.

With this information and using an offline version of the CrIS SDR processing system, the next step was to estimate the time to process one dwell using 1 CPU. For this estimate, 12 test cases were run on existing hardware at NOAA/NESDIS/ Center for Satellite Applications and Research (STAR). For each test case, 4 dwells were processed simultaneously using 1 CPU per dwell, where each CPU processed 48 050 interferograms independently. As shown in Table IV, the data processing time values are consistently close to 560 s for each test case. This means that it is possible to process 56 dwells in about 10 min.

Based on the hypothetical scan configuration, a FD consists of about 350 GEO-HyIRS dwells. Thus, approximately 1 h is needed to process all the dwells within a FD. These results are the basis for the notional GEO-HyIRS data processing configuration presented in Fig. 4, where dwell data is sequentially fed into the ground data processing system servers, consisting of 224 CPUs, for multiprocessing. Each dwell of data is processed by 4 CPUs in parallel so that its data processing can be finished in 2.5 s. This configuration aims at processing 56 dwells in less than 2.4 min (one cycle) using 224 CPUs working simultaneously. This processing time is in line with the latency requirement of the GXS sensor, which is expected to be less than 5 min [34]. Under

TABLE V
PROXY PRODUCT DATA VARIABLE DIMENSIONS

Horizontal Spatial Resolution		Full Disk		CONUS Extraction from Full Disk		CONUS		Mesoscale	
km (nadir)	micro-radians	E/W (x-axis)	N/S (y-axis)	E/W (x-axis)	N/S (y-axis)	E/W (x-axis)	N/S (y-axis)	E/W (x-axis)	N/S (y-axis)
4.0	112	2712	2712	752	752	752	752	250	250
16.0	448	678	678	188	188	188	188	125	125

this notional parallel processing configuration, it is expected that 349 GEO-HyIRS dwells, approximately a FD, as shown in Table III, will be processed in about 15 min (approximately 6 processing cycles, as shown in Fig. 4). Designing a system to process the dwells within a specific latency is out of scope of this article. If more CPUs can be configured, the data processing time can be further reduced.

V. SIMULATOR TO CREATE GEO-HYIRS PROXY DATA

A software simulator was developed to produce GEO-HyIRS proxy data using CrIS observations. Data from the simulator enables the design and testing of an end-to-end data processing system on the ground. It should be noted that while the CrIS spectral bands are slightly different from those defined for the notional GEO-HyIRS instrument in Table II, the proxy data simulated from CrIS is a close approximation of a GEO-HyIRS sensor, including the spectral resolution and number of channels per spectral band.

A. Simulated GEO-HyIRS Proxy Radiance Data

There are two methods to generate the proxy radiance for the notional GEO-HyIRS. The first method is to use a forward model such as the CRTM [41], [42] with NWP model forecast fields, i.e., the atmospheric and surface conditions, as input, and to simulate the observations at the GEO-HyIRS field-of-view under clear- and cloudy-sky conditions. The second method consists of using existing hyperspectral infrared sounder observation data collocated with the GEO-HyIRS observation locations (fixed grid) [36]. In this engineering study, we used the second method to generate the synthetic GEO-HyIRS proxy data, using S-NPP and NOAA-20 CrIS SDR products at FSR (2211 channels at 0.625 cm^{-1} spectral resolution) on polar-orbit satellites.

The geolocation products from ABI are in a fixed grid [36]. The fixed grid is a projection based on the viewing perspective of the idealized location for a given satellite in a geosynchronous orbit. The horizontal spatial resolution was defined by the angular separation of the data points on the fixed grid. The angular separation of the data points includes the East to West (E/W) (x-axis) scanning angle and the North to South (N/S) (y-axis) elevation angle. The North to South and East to West coverage range on the fixed grid for the full disk products is 17.4° for GOES-16. Table V lists the proxy data dimensions, nadir horizontal spatial resolution, angular separation, as well as different interesting domains.

We first obtained one full day of CrIS SDR and RDR data on S-NPP and NOAA-20 and then obtained ABI L1B data on GOES-16 (projected to 75 W longitude) with UTC time from 6:00 P.M. to 7:00 P.M., and from 6:00 A.M. to 7:00 A.M. This corresponds to the Local Equator Crossing Time (LECT) at 13:30 P.M. for the ascending node and at 1:30 A.M. for the descending node for both S-NPP and NOAA-20, respectively. To determine the geodetic latitude/longitude coordinates, the fixed grid coordinates, based on a given horizontal spatial resolution, N/S elevation angle, and E/W scanning angle are coupled with the location of the satellite (assuming the GEO-HyIRS satellite geospatial nadir is located at the GOES-east position) and the parameters associated with the Geodetic Reference System 1980 (GRS80). With each GEO-HyIRS latitude/longitude, we can find the nearest pixel from the CrIS geolocation product. The CrIS scans a 2200 km swath width, which is not wide enough to cover the whole globe with notable observation gaps found between orbits at the tropical regions. When using only observations from one CrIS sensor to generate the proxy data, spatial gaps exist in the generated full disk data. The spatial gaps can be filled by using neighboring pixels or by combining the observations from both the S-NPP and the NOAA-20 CrIS sensors. One drawback of using neighboring pixels to fill the gap is that the data would have artificial strips in the filled gaps. In this article, we decided to use observations from both the S-NPP and NOAA-20 CrIS sensors to fill the spatial gap. Both CrIS instruments have LECT at 13:30 P.M., but are separated in time by approximately 50 min (or about half orbit).

The proxy data was generated using the CrIS observations closest to the hypothetical GEO-HyIRS fixed grid and keeping key sensor information from both S-NPP and NOAA-20 at each fixed grid. This key information would be later used in Section V-B to generate geophysical products. Fig. 5 shows an example of the GEO-HyIRS full disk proxy data at the 968.125 cm^{-1} channel generated using observations of only one CrIS [see Fig. 5(b)] and two CrIS instruments [see Fig. 5(c)] as well as the observations from the GOES-16 ABI channel 13 [see Fig. 5(a)].

B. EDR Geophysical Testing Using the Simulated SDR

A variety of operational sounding products from hyperspectral IR observations are produced using the NOAA Unique Combined Atmospheric Processing System (NUCAPS). Operational sounding products from the NUCAPS system include the atmospheric vertical profiles of temperature, water vapor, ozone, and trace gas products (CO, CH4, and CO) from the CrIS and IASI aboard the JPSS (S-NPP/NOAA-20) and MetOp (MetOp-A, B, C) series of polar orbiting satellites, respectively.

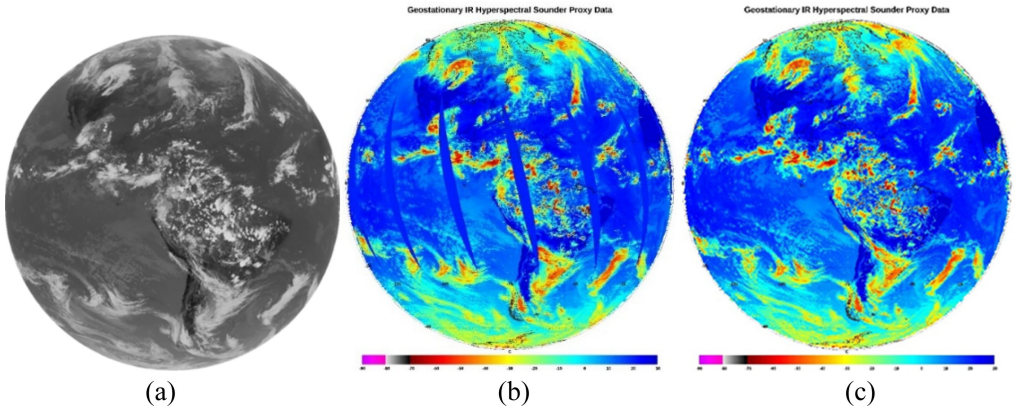

Fig. 5. GEO-HyIRS proxy data based on observations from the CrIS sensor. (a) Observations from the GOES-16 ABI channel 13 with center wavenumber of 968.125 cm^{-1} on October 20, 2019 from 18:30 to 18:40 UTC and with spatial resolution of 2 km at nadir. (b) GEO-HyIRS proxy data at 968.125 cm^{-1} with spatial resolution of 16 km, based on the S-NPP CrIS SDR product from October 20, 2019 at about 18:30 UTC. (c) Same as (b), but combining observations from the S-NPP and NOAA-20 CrIS sensors to fill presence of observation gaps found when only one CrIS sensor is used.

The algorithm, built on the heritage from the AIRS science team algorithm [43], uses the microwave sounder radiances from ATMS or AMSU-A/MHS sensors aboard the respective satellite platforms to produce microwave-only retrievals and QC/QA flags as a front-end to the hyperspectral IR sounding physical retrievals. The downstream retrieval step replaces the front-end microwave-only retrieval by a fast eigenvector regression trained with the collocated forecast-analysis-interpolated ECMWF and all sky hyperspectral infrared (IR) radiances. The fast eigenvector regression solution generates the first guess profiles of temperature and water vapor [44]. A cloud clearing module uses observed radiances of a set of channels from adjacent n x n FOVs ($n = 3$ for CrIS and $n = 2$ for IASI) to specify a cloud-cleared radiance for all channels. A second fast eigenvector regression that is trained with the collocated forecast-analysis-interpolated ECMWF and cloud cleared radiances provides the initial solution to the final IR physical retrieval. The final step uses an iterative physical retrieval algorithm to produce the final Level-2 retrieval products. The NUCAPS Algorithm Theoretical Basis Document [45] available online provides a detailed discussion on the functioning of various components, and the use of the fast IR radiative transfer model, also known as the Stand-Alone AIRS-Radiative Transfer Algorithm [46]. The NUCAPS EDR products have been validated using a well-established validation methodology and utilizing a variety of model outputs (e.g., ECMWF), products derived from other satellite sensors (e.g., AIRS, TROPOMI, and *in situ* measurements [47]–[50].

Assuming no geostationary microwave sensor companion for the GEO-HyIRS, NOAA/NESDIS/STAR has adapted an offline version of the NUCAPS IR-only algorithm for the GEO-HyIRS with necessary modifications to the algorithm subcomponents such as: the surface characterization, the all-sky eigenvector regression retrieval, the cloud-clearing algorithm, and the second eigenvector regression, to generate the necessary first guess for the final IR-only physical retrieval. The flowchart in Fig. 6 shows the components of NUCAPS Level-2 product retrieval system for GEO-HyIRS. Apart from static ancillary Lookup Tables (LUTs) or processing coefficient files (PCF) available as part of the current NUCAPS algorithm (Ozone,

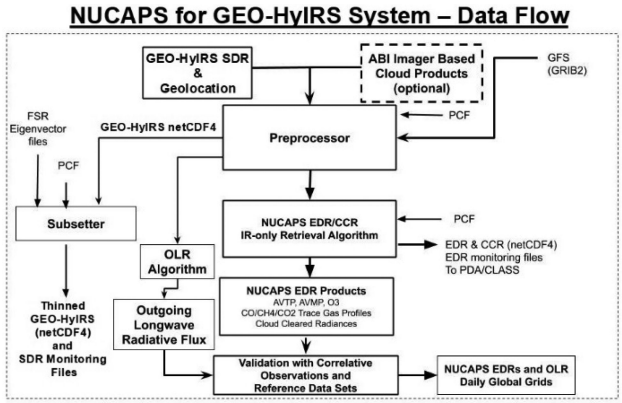

Fig. 6. Components of NUCAPS Level-2 product retrieval system for the GEO-HyIRS. The PCF represent the system static ancillary data, while the GFS model data, along with the geolocated GEO-HyIRS simulated radiances in the form of SDR product, represent the only input dynamic data needed by the NUCAPS system.

CO, CH_4, CO_2, N_2O, HNO_3, and SO_2 a-priori profile LUTs, CrIS sensor noise and fast-forward model LUTs, regression LUTs for all-sky and cloud-cleared regression, land surface spectral emissivity first guess LUT), the IR-only algorithm requires only two dynamic inputs: 1) the GEO-HyIRS proxy sounder radiances; and 2) the surface parameters from the Global Forecast System (GFS) model data. The GFS surface pressure, ice concentration and snow depth are included as dynamic inputs to replenish the absence of microwave-sensor related quality checks and quality assurance (QC/QA) and to improve the boundary layer characterization.

The offline NUCAPS IR-only retrieval algorithm has been applied to the GEO-HyIRS proxy data derived from the S-NPP and NOAA-20 CrIS SDR data products, as shown in Fig. 5(c). Sensor specific LUTs and static ancillary LUTs specifically made for the IR-only configuration were used with the GEO-HyIRS proxy data to retrieve atmospheric profiles of temperature, water vapor, and trace gas products at a FOR resolution of 3 × 3 GEO-HyIRS FOVs. Fig. 7 shows a comparison of the NUCAPS GEO-HyIRS IR-only temperature and water

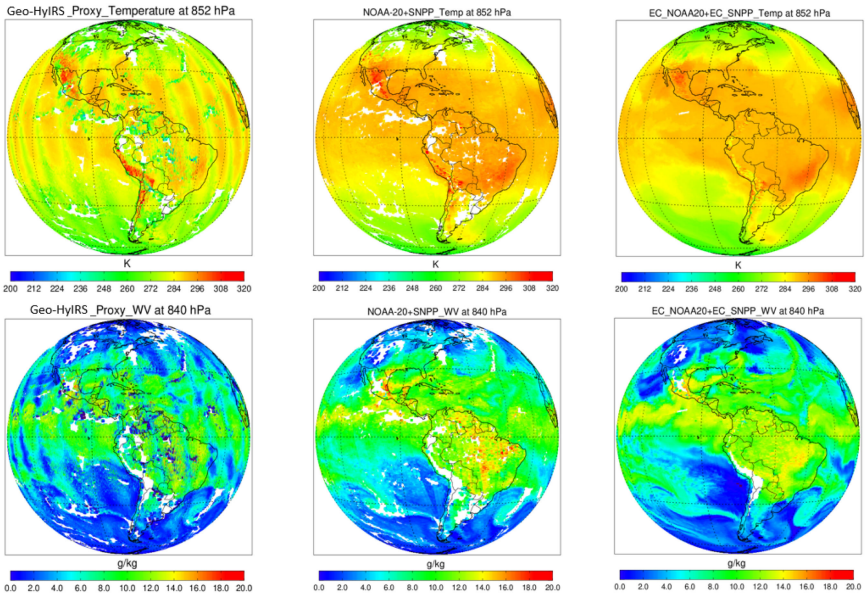

Fig. 7. NUCAPS GEO-HyIRS IR-only retrieval of temperature at 852 hPa and water vapor at 840 hPa (left-maps) as well as the corresponding NUCAPS IR-only retrievals resulting from combining the operational NOAA-20 and S-NPP CrIS observations (middle-maps), and the ECMWF forecast-analysis-interpolated temperature and water vapor fields collocated with NOAA-20 and S-NPP CrIS observations (right-maps). White areas correspond to regions associated with high elevation or low atmospheric pressure. In the case of NUCAPS retrievals (left and middle maps), the white areas also correspond to regions associated with conditions where the NUCAPS system is unable to converge to a physical solution, including high precipitation conditions or difficult cloud cases.

vapor retrievals (left-maps) against both the NUCAPS IR-only retrievals based on the operational NOAA-20 and S-NPP CrIS observations (middle-maps) and the corresponding matched ECMWF forecast-analysis temperature and water vapor fields (right-maps). The figure reveals that the GEO-HyIRS IR-only retrievals (see Fig. 7, left-maps) are qualitatively comparable (higher temperatures and water vapor content near the tropics) to the NUCAPS S-NPP/NOAA-20 IR-only retrievals (see Fig. 7, middle-maps) and ECMWF fields (see Fig. 7, right-maps). The main purpose of these results is to demonstrate and test the capability to generate Level-2 products using the NUCAPS system applied to the GEO-HyIRS proxy data, in order to support the modeling of the end-to-end ground data processing system. The main reason for the orbital patterns shown in the NUCAPS GEO-HyIRS IR-only retrieval results is associated with the method used to fill the spatial gaps during the generation of the GEO-HyIRS proxy data, discussed in Section V-A. In this case, the effect of the different observation viewing angles of S-NPP and NOAA-20 CrIS are more evident over those regions where low spatial overlap between S-NPP and NOAA-20 CrIS observations is found [basically over the orbital gap regions identified in Fig. 5(b)]. This effect creates the orbital patterns observed in the retrieved NUCAPS GEO-HyIRS temperature and water vapor fields shown in Fig. 7 (left maps).

VI. GEO-HyIRS Design and Calibration/Validation Considerations

A. Calibration and Validation Methodology for the GEO-HyIRS

The overall methodology of the calibration and validation of the GEO-HyIRS sensor will be inherited and developed from the calibration and validation of the existing and planned LEO/GEO infrared sounders and GEO imagers. The calibration methodology of the operational CrIS and IASI sensors is studied as reference for the calibration of the GEO-HyIRS. Intersensor comparisons are reported to discuss the advantages and disadvantages of increasing on-board data processing. In this article, the IASI and CrIS (reprocessed version 2) results are used to highlight the importance of performing on-ground data processing.

The CrIS GS configuration responsible for the processing of downlinked L0 data to the calibrated L1B SDR is described in detail in Section IV-A. On the other hand, the configuration employed for the production of calibrated IASI radiances makes use of more on-board data processing prior to data downlink. The IASI instrument measures continuous spectra from 645 to 2760 cm^{-1} with an apodized spectral resolution of 0.5 cm^{-1}, resulting in 8641 radiance measurements per spectra compared to the 2211 channels observed by CrIS when operating in FSR mode. To reduce the downlink data rate for IASI by roughly a factor of 30, the processing from raw interferograms to calibrated radiance spectra is carried out on-board the satellite [51]. These calibrated spectra are downlinked to a GS where they are further processed to yield fully calibrated and geolocated spectra as well as ancillary parameters, including cloud fraction. The raw measurements of the instrument are discarded except during certain scenarios, such as when the instrument is operating in calibration modes.

While this approach has the advantage of reducing the downlink data rate, it introduces several disadvantages. First, on-board data processing and calibration require that more complex hardware be housed on-board the satellite. The additional memory and other electronics needed to perform the computations are

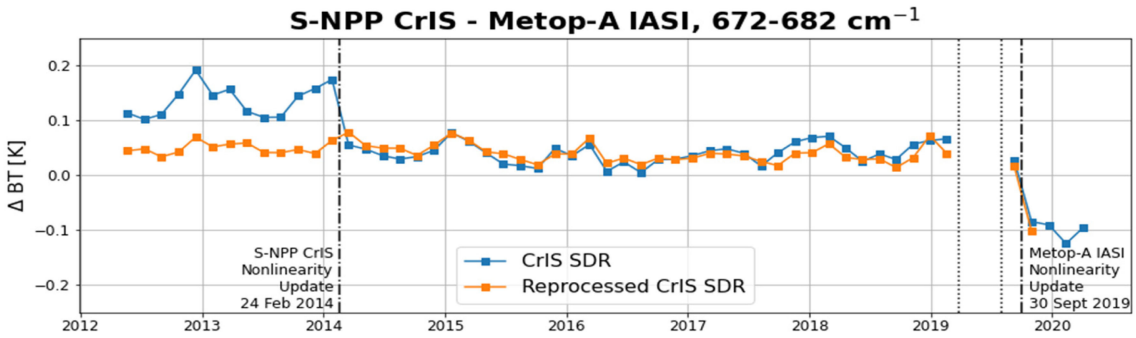

Fig. 8. Mean brightness temperature bias between S-NPP CrIS and Metop-A IASI averaged over the spectral region 672–682 cm^{-1} for the operational near-real time CrIS SDR product (blue curve) and the reprocessed version 2 CrIS SDR product (orange curve).

all potentially vulnerable to the radiation environment of a GEO orbit. Any corruption or loss of data during the processing is permanent. Furthermore, when a significant portion of the data processing is conducted on-board and only calibrated spectra are downlinked, there is limited ability to reprocess the data to eliminate discontinuities. Updates to either calibration algorithms or parameters create discontinuities in the instrument performance across the mission data record. Ground-based processing using downlinked interferogram data, as is implemented for CrIS, allows for the option to fully reprocess the SDR product at a later date using a consistent set of calibration equations and parameters to produce a dataset with consistent performance across the historical record. Such datasets have advantages for climate and reanalysis applications because artifacts that are introduced as a result of the calibration changes are eliminated. The benefits of being able to reprocess the data are illustrated in Fig. 8. This result shows time series of brightness temperature biases between Suomi NPP CrIS (operational and reprocessed) and Metop-A IASI averaged over the spectral region from 672 cm^{-1} to 682 cm^{-1} when the two instruments experience simultaneous nadir overpasses (SNOs). The IASI spectra are resampled onto the CrIS spectral grid, and each point represents the bias between collocated CrIS and IASI FOVs averaged over the roughly 24 northern hemisphere SNOs that occur every ∼50 days for these two satellites.

A nonlinearity correction update was implemented for the operational S-NPP CrIS SDR product on February 20, 2014. A shift in the bias of the operational CrIS SDR data product produced in near real time with respect to Metop-A IASI, indicated by the blue curve, can be seen. The shift in bias is eliminated when comparing Metop-A IASI to the S-NPP CrIS SDR reprocessed dataset (orange curve), resulting in a more consistent bias trend across the mission data record. A nonlinearity correction update was applied to Metop-A IASI in September of 2019, resulting in a shift in the bias with respect to S-NPP CrIS. Since limited raw interferogram data are downlinked from IASI instruments, it is not possible to reprocess the IASI data to eliminate this discontinuity.

It is desirable to downlink the raw data and complete the calibration using ground-based processing to maintain the option to reprocess the data in the future, using consistent calibration algorithms and parameters and reduce the complexity of the on-board hardware. While on-orbit data processing can reduce the downlink data rate requirements, the raw data needed for diagnostic and reprocessing capabilities is lost.

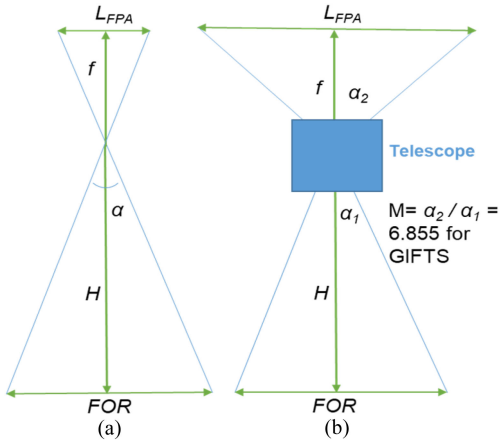

Fig. 9. Schematic of the focal plane array geometry of a sensor based on an afocal ratio, M of (a) $M = 1$ and (b) $M = 6.855$. The figure is for illustration purposes. The dimensions are not to scaled.

B. Evaluation of Large Spectral Shifts Associated With the GEO-HyIRS

The large detector array expected for a GEO-HyIRS sounder will induce challenges during the calibration process. One example of that is related to the spectral calibration where the quality heavily relies on the accurate knowledge of the sensor focal plane array (FPA) geometry, including the detector's OFF-axis angle, the detector angular size, and the focal length. Based on Fig. 9(a), the detector angular size α of a GEO-HyIRS FPA could be determined by

$$\frac{L_{\mathrm{FPA}}}{f} = \frac{\mathrm{FOR}}{H} \approx \alpha \tag{1}$$

where α represents the detector angular size in units of radians, f is the focal length, and H is the satellite height.

In (1), the calculation of the detector angular size is based on a greatly simplified model. In reality, the instrument telescope, an afocal system, magnifies the detector angular size

TABLE VI
SPECTRAL SHIFT COMPARISON BETWEEN THE GEO-HYIRS AND CRIS SENSORS. FOR THE GEO-HYIRS SENSOR, A DWELL OF 155 × 155 DETECTORS IS USED. THE ABI (M=1) AND GIFTS (M=6.855) FORE-OPTICS WERE USED AS REFERENCES IN THIS ANALYSIS. A DETECTOR ANGULAR SIZE OF 112 μRAD AND 766 μRAD IS ESTIMATED FOR A GEO-HYIRS CONFIGURATION BASED ON AN AFOCAL RATIO OF M=1 AND M=6.855, RESPECTIVELY. THE CRIS SENSOR HAS 3×3 DETECTORS, EACH ONE WITH ANGULAR SIZE OF 16808 μRAD

	700 cm^{-1} (cm^{-1})	1210 cm^{-1} (cm^{-1})	1590 cm^{-1} (cm^{-1})	2250 cm^{-1} (cm^{-1})	Spectral shift (ppm)
GEO-HyIRS/ Center, M=1	0	0	0	0	0
GEO-HyIRS/ Corner, M=1, Without gap *	0.0524	0.0905	0.1190	0.1683	74.82
GEO-HyIRS/ Corner, M=1, With Gap**	0.0679	0.1174	0.1543	0.2183	97.02
GEO-HyIRS/ Center, M=6.855	0.000028	0.000048	0.000064	0.000090	0.04
GEO-HyIRS/ Center, M=6.855, Without gap*	2.4382	4.2145	5.5381	7.8369	3483.07
GEO-HyIRS/ Center, M=6.855, With gap **	3.1682	5.4765	7.1964	10.1836	4526.03
CrIS/ center	0.0124	0.0214	0.0281	0.0397	17.66
CrIS/ corner	0.2691	0.4652	0.6113	0.8650	384.44

*Without gaps between detectors.
**With gaps between detectors, ratio to angular size: 1.14.

according to

$$\frac{L_{\mathrm{FPA}}}{f} \approx \alpha_2 = M\,\alpha_1 = M\left(\frac{\mathrm{FOR}}{H}\right) \tag{2}$$

where M represent the magnification of the system or afocal ratio. Using (2), the GIFTS value of $M = 6.855$ as a reference [52] for the GEO-HyIRS, a FPA configuration with 155×155 detectors and a 4 km nadir spatial resolution, the corresponding GEO-HyIRS FPA angular size can be approximated by $\alpha_{\mathrm{FPA\_GEO1}} \approx 6.855 \times 155 \times 4$ km / 35 800 km $= 0.119$ rad, and the detector angular pixel size by $\alpha_{d\_GEO1} \approx 6.855 \times 4$ km / 35 800 km $= 766$ μrad. If using the ABI optics design, where $M = 1$, the FPA and detector angular size of the GEO-HyIRS sensor would be $\alpha_{\mathrm{FPA\_GEO2}} = 0.017$ rad and $\alpha_{d\_\mathrm{GEO2}} = 111.7$ μrad, respectively. For reference, the CrIS FPA and detector angular size are 0.056 rad and 16908 μrad, respectively.

Using the methodology described in [37], the expected spectral shift, in wavenumber and ppm, as a function of wavenumber and for two optical design configurations ($M = 1$ and $M = 6.855$), is reported in Table VI. For this analysis, we consider a blackbody emission with temperature at 280 K. For comparison purposes, the spectral shift is computed for the GEO-HyIRS detector located in the center and corner of the sensor FPA. The corresponding CrIS spectral error is included as reference. As expected, results in the Table VI show that the largest spectral shift is observed at the corner detectors due to the largest OFF-axis angle associated with these detectors.

A large afocal ratio, or angular magnification of the telescope, $M = 6.855$ is adopted by GIFTS as a system trade to shrink the size of the incident light to fit the aperture of the interferometer. When comparing the impact of the detector angular size, it is clear that the spectral shift is significantly larger for the sensor with larger M value. Actually, the spectral shift of the notional GEO-HyIRS based on an afocal ratio of 6.855 is expected to be about one order of magnitude larger than the spectral shift observed for the CrIS sensor. However, the correction of those large spectral shifts is very well understood and is based on a rigorous mathematical process that relies on the knowledge of the geometry of the FTS. Due to that, it is expected that those large spectral shifts are corrected to the level of a few ppm, during the spectral calibration process. In fact, due to the small size of the GEO-HyIRS detectors (pixel angular size of about 112 μrad) compared to large detector size of sensors like CrIS (pixel angular size of 16908 μrad), the beam divergence effect introduced by the detector size should be less in the GEO-HyIRS case, reducing the complexity of the self-apodization correction process. Depending on the design constraints, the actual GEO-HyIRS telescope system could also be further optimized to reduce the maximum spectral shift before correction. Some advantages of having an afocal ratio greater than one are related to size, volume, and cost reduction as well as temperature control benefits.

C. Radiance Spectra Compression Using Principal Component Compression

In a further effort to reduce the data volume of high spectral resolution sensors, additional data processing can be employed to compress the calibrated spectra either on-board the satellite prior to downlink or during the ground-based data processing prior to distribution to users. On top of lossless compression techniques studied for hyperspectral sounder data [53], PCC has been widely applied to the output radiance spectra of hyperspectral infrared sounders, such as the currently operational AIRS and IASI [44], [54], and is expected to be used by the planned MTG-IRS and IASI-Next Generation (NG) instruments.

PCC is essentially a technique to reduce the dimensionality of a dataset x, by identifying a subset of orthogonal basis vectors with which to represent the data, such that the most significant information content of the dataset is retained. The orthogonal basis vectors are obtained by diagonalizing the covariance matrix of the noise-normalized dataset recentered about its mean. When PCC is applied to spectra, x represents the observed spectra L, with dimensions of $p \times m$, where p is the number of samples and m the number of channels. In this case, the noise matrix $\boldsymbol{N}$ has dimensions of $p \times p$. Thus, the normalized matrix $\boldsymbol{X}$ can be defined as

$$\boldsymbol{X} = \boldsymbol{N}^{-1}\,(x - \bar{x}) \tag{3}$$

where $\boldsymbol{N}\bar{x}$ represents the mean of the noise normalized dataset x. Principal component analysis (PCA) is conducted as the eigenvector decomposition of the covariance matrix of the radiance dataset, given in the form of the normalized matrix

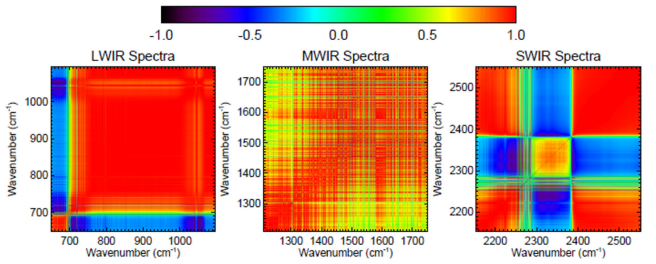

Fig. 10. Correlation coefficients among spectral channels of CrIS spectra within a band, calculated from an orbit of S-NPP CrIS SDR from July 27, 2020.

($\boldsymbol{X}$), as follows:

$$\boldsymbol{S} = Cov(\boldsymbol{X}) = \boldsymbol{X}\boldsymbol{X}^{\boldsymbol{T}} = \boldsymbol{E}\boldsymbol{\Lambda}\boldsymbol{E}^{\boldsymbol{T}} \tag{4}$$

where $\boldsymbol{E}$ and $\boldsymbol{\Lambda}$ are the eigenvectors, or principal components (PC), and eigenvalues matrices, respectively. The variance represented by each PC is given by the corresponding eigenvalue. The compression is achieved by using a truncated set of s PCs, leading to PCs with the largest variances to represent the original dataset as

$$\boldsymbol{Y}^{*} = \boldsymbol{E}^{*\boldsymbol{T}}\,\boldsymbol{X} = \boldsymbol{E}^{*\boldsymbol{T}}\boldsymbol{N}^{-1}(x - \bar{x}) \tag{5}$$

where $\boldsymbol{E}^{*}$ represents the truncated eigenvector matrix with dimension $m \times s$ and $\boldsymbol{Y}^{*}$ is the dataset of PC scores with dimension $s \times p$, which is reduced compared to that of the original dataset.

It is known that hyperspectral infrared observations are highly correlated in the spectral domain. To illustrate this, the correlation coefficients among spectral channels are calculated using one randomly selected orbit of S-NPP CrIS radiances measured on July 27, 2020 from 00:00 to 01:40 UTC (see Fig. 10). This result implies that the atmospheric information found in hyperspectral infrared observations can be represented using a reduced set of PCs. The application of PCA to compress high spectral resolution observations has been previously studied [55], showing that PC compression can reduce the observation data volume significantly, while retaining critical atmospheric information.

There are a number of methodologies for selecting the PC truncation point such that the retention of atmospheric signal is optimized [56]. The ratio of the data volumes of $\boldsymbol{X}$ and $\boldsymbol{Y}^{*}$, given by m/s, is the compression ratio. As reference, a summary of available information of PCC parameters and compression ratios of existing or planned hyperspectral infrared sensors, including AIRS, IASI, IASI-NG, and MTG-IRS, is listed in Table VII.

The reconstruction of the radiance spectra from the PC scores is performed using the same set of eigenvectors, noise matrix, and mean radiance used in the PC compression

$$\tilde{\mathrm{x}} = \boldsymbol{N}\mathbf{E}^{*}\,\mathbf{Y}^{*} + \bar{x} \tag{6}$$

where the reconstruction static components are represented by the matrices $\boldsymbol{N}$, $\boldsymbol{E}^{*}$, and $\bar{x}$, while the reconstruction dynamic component is represented by the PC scores ($\mathbf{Y}^{*}$). In this case, the dynamic component, given in the form of PC scores, is disseminated to data users, which typically allows data compression rates close to 10 or more.

TABLE VII
EXAMPLES OF REMOTE SENSING INSTRUMENTS WITH PCC

	AIRS	IASI Band 1/2/3	IASI-NG Band 1/2/3/4	MTG-IRS LWIR/ MWIR
Number of Spectral Channels (m)	2378	2261/3160/ 3040	4040/6480/ 2480/3921	817/921
Number of PCs (s)	200	90/120/80	100/100/80/60	150/150
Compression Ratio (m/s)	12	25/26/38	40/65/31/65	5.5/6

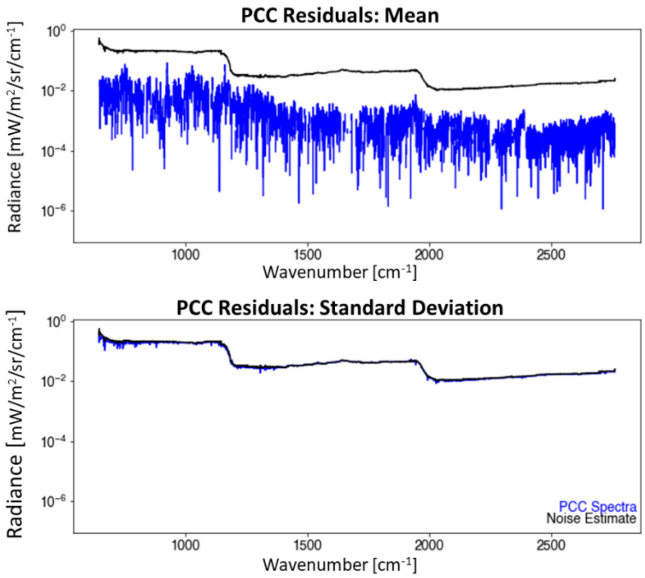

Fig. 11. Mean (top) and standard deviation (bottom) of residuals between the observed Metop-C IASI radiances and the PCC reconstructed radiances over all scenes observed on April 30, 2020 (blue curve). The IASI radiometric noise is included as reference (black curve).

The portions of the spectra that are lost as a result of the compression are called radiometric residuals and are given by $\hat{x} = x - \tilde{x}$. When the PCC parameters are well chosen, including the noise estimate used to normalize the data, this technique has the added benefit of filtering the random instrument noise present in the observed radiances [57].

Observed and reconstructed spectra from Metop-C IASI were used to illustrate some characteristics of the radiometric residuals, $\hat{x}$**.** The mean and standard deviation of the residuals for the more than one million Metop-C IASI spectra observed on April 30, 2020 are shown in Fig. 11. The reconstructed PCC spectra are obtained from the PC scores product distributed by EUMETSAT and compared to the L1C radiance product. The sensor noise estimate used in the compression and reconstruction is indicated by the black curve. As shown in Fig. 11, the magnitude of the mean radiometric residual is small compared to the sensor noise, while the standard deviation of those residuals closely matches the noise estimate, suggesting that the residuals are mostly comprised of radiometric noise. Thus, the reconstructed

radiances retain the atmospheric signal and the resulting radiometric residuals consist mostly of noise.

D. Interferogram Compression: An Alternative Principal Component Compression Approach

For a GEO-HyIRS based on a Michelson Interferometer design, the downlink data rate is mainly dominated by the large data volume needed to transmit the measured interferograms to the ground stations. Based on the estimations provided in Section III, a data rate close to 100 Mb/s will be required. Similar to CrIS, this data rate includes compression on-board, associated with interferograms decimation and the application of the bit-trim compression. The downlink data mainly includes interferograms in their complex form (real and imaginary components). Based on the data compression listed in Table VII, applying PC compression could help to reduce the GEO-HyIRS downlink data rate to close to 10 Mb/s.

Traditionally, the PCC is applied to the calibrated radiance spectra as part of the ground data processing. However, as discussed earlier, downlinking interferograms as opposed to calibrated radiances is preferable to retain the diagnostic and reprocessing capabilities. Additionally, many users with low latency requirements rely on direct broadcast data and would not benefit from the reduced data volume realized by ground-based processing of PCC radiances. Direct broadcast data are highly important for regional weather forecast applications, including nowcasting, due to the low latency associated with this type of data [58].

Since the GEO-HyIRS is expected to benefit applications that require low latency, including short-term weather forecasting, while efficiently overcoming some limitations associated with the downlink capacity, in this article, we explore the application of on-board PCC to measured interferograms I directly as a means of reducing the downlink data rate of the GEO-HyIRS sensor. The feasibility of the interferogram PCC is tested using CrIS data as proxy. The CrIS measured interferograms (IGMs) are digitally filtered, decimated, and bit-trimmed on-board. Then, those compressed interferograms are downlinked and repackaged into the form of RDRs, as described in Section IV-A. As part of this article, an orbit of S-NPP CrIS RDRs from July 27, 2020 was selected as the baseline dataset. This is the same dataset used to generate the correlation coefficients presented in Fig. 10. For each band, the selected dataset consisted of approximately 200 000 ES FOVs. The CrIS Interferometry Transformation System (CITS) was used to process the RDR data and produce calibrated radiances in the form of SDR data. The CITS system has similar capabilities to the Interface Data Processing Segment, which is used to generate operational CrIS SDRs. It should be noted that the noise of the IGMs is not characterized and the PCC of spectra is conducted without the noise normalization.

The variance in the data along the PC direction is represented by the eigenvalue λ from the PCA. In this respect, Fig. 12 helps to illustrate the variance loss (expected during the PC compression) when different numbers of PCs are preserved for the observed spectra L and the measured interferograms I.

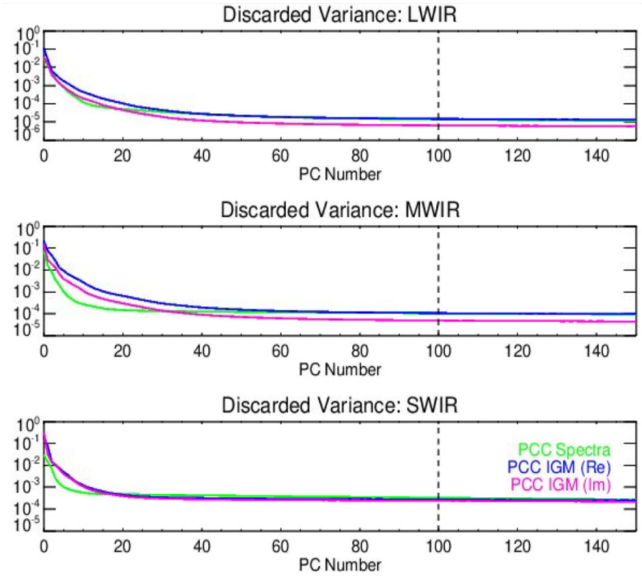

Fig. 12. Relative loss of variances during the PCC for the SDR spectra, and the real and imaginary parts of the associated IGMs.

In the case of the interferograms I, the PC compression is applied to the real and imaginary parts, separately, so two sets of eigenvalues are calculated and plotted. The variances of I and L are not in the same units, so the discarded variance is normalized to the total variance and it is the relative amount of loss that is plotted here. The rapid drop of the information loss indicates that most of the information can be preserved by the leading PCs. Compared to the eigenvalues of I, Fig. 12 shows that the eigenvalues of L drop much faster. When the PC ranks are higher, the eigenvalues of L decrease less rapidly, until their values become greater than the corresponding values of I so that the loss of variance due to the PCC of I and L are comparable. Therefore, it is possible to use the same or similar number of PCs to preserve comparable amounts of variances for I and L. Based on the analysis of the performance of the L and I eigenvalues, it was decided to keep the first 100 PCs for the compression in the spectral and interferogram domain in the following tests. The value of 100 eigenvalues is also very similar to the eigenvalue cutoff used for the PC compression of existing hyperspectral infrared sounders [44], [59].

The performance of calibrating the PCC IGM is further assessed in the following test. Two sets of PCC compressed spectra using the same number of PCs were generated: set I by PCC compressing the calibrated spectra L directly and set II by calibrating the PCC compressed I. The reconstruction of I and L is based on (6). The uncompressed spectra L is then subtracted from the reconstructed spectra of set I, L'_1, and set II, L'_2, to calculate the PC reconstruction residuals $L'_1 - L$ and $L'_2 - L$. The residual is then a quantitative measure of the information lost during PCC. Fig. 13 shows the absolute of the mean value and the standard deviation of the PC reconstruction residuals per spectral channel. As reference, the on-orbit S-NPP CrIS NEdN has been included. For the mean value results, the absolute value is computed and plotted to fit into a Logarithmic scale chart.

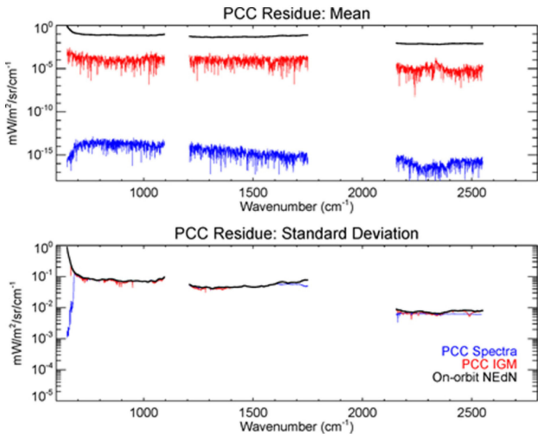

Fig. 13. (Upper panel) absolute mean value and (lower panel) standard deviation of the PC reconstruction residual.

This result clearly shows that the mean values are very close to zero for both sets of radiometric residuals, indicating the PC reconstruction residuals are extremely small and consistently below the sensor NEdN. The standard deviations of the radiometric residual closely match the on-orbit NEdN of the instrument, the value of which itself is derived with a PCA approach, similar to the PC reconstruction residual [60]. This confirms that the data information loss during the PCC IGM is basically noise, a fact that is well known from the study of PCC spectrum. Fig. 13 shows that the standard deviation of the PCC spectra radiometric residual approaches to zero for wavenumber values closer to the lower edge of the LWIR band. Since this effect occurs over a spectral region where the nonlinearity correction is particularly large, it is possible that the detector nonlinearity correction applied as part of the CrIS calibration process contributes to this effect. The exact reasons of this observed effect have not been fully investigated.

Since the information discarded by the PCC is mostly noise, the radiance that contains the useful information about the Earth scene is mostly preserved during the PCC process, as expected. There are several factors to consider for actual implementation of IGM PCC on-board: the measured IGMs, output from the sensor interferometer, will consist of only real signals, since the PC compression will be applied before the digital filtering. This eliminates the need to compress the real and imaginary components of the complex interferograms separately. In addition to that, it is possible to apply bit-trim compression to the PC scores to further reduce the downlink data rate. This is because the dynamic range of each PC, which is determined by the corresponding eigenvalues, decays very rapidly with the increase of the PC rank. The dynamic range for most of the preserved PCs is extremely small, as shown in Fig. 12, and can be represented with fewer bits than those very few PCs associated with the largest information content. The numbers of PCs to conduct PCC can also be optimized. Additionally, the noise normalization, a process required for the PCC of radiance spectra, is not needed for the PCC of the IGMs since the noise levels of the IGM samples are nearly the same for a given short period of time.

E. Potential Lunar Calibration and Validation Capabilities

In addition to the radiometric intersensor comparisons using earth SNOs, lunar observations could potentially add the capability to further assess the radiometric and geometric stability of the GEO-HyIRS sensor. The moon can enter the FOR of the instrument multiple times every month at 8°–12° phase angles, acting as a free calibrator without satellite maneuver involved. It can be observed by the detectors either for the dwell measuring the space background during normal operation, or for dwells specially designed for lunar calibration and validation activities. As presented in Section VI-B, the planned 4 km nadir spatial resolution of the GEO-HyIRS corresponds to approximately 111.7 μrad instantaneous FOV. Thus, the full moon disk will be spanned by about 80 image pixels in diameter. This is about half of the spatial resolution of the observations at the GOES-R ABI IR bands and about 4 times the spatial resolution of the observations made by the JPSS Visible Infrared Imaging Radiometer Suite (VIIRS) imagery bands I1-I5.

Well-established lunar calibration and validation strategies for MODIS, VIIRS, and ABI instruments can be used as reference for the GEO-HyIRS calibration and validation. For example, proxy GEO-HyIRS lunar images can be generated from CrIS data for preliminary assessment. Lunar observations could be used to support the characterization of the instrument geometric factors, such as band-to-band registration (BBR), detector-to-detector registration (DDR), and modulation transfer function (MTF) [61], critical for a GEO-HyIRS design with large FPAs.

The BBR and DDR are calculated from the shift of centroids among the lunar images of different bands and detectors. The MTF can be derived from the edge of the moon. However, absolute IR calibration will still primarily reference an on-board blackbody. The extension of robotic lunar observatory (ROLO) model to IR region with reasonable accuracy would be the key for potential absolute lunar IR calibration. A recent study reported in [62] is attempting to demonstrate the potential use of lunar observations for the radiometric calibration of infrared sounders using IASI. In addition to that, lunar observations also have the potential to independently track the radiometric calibration stability, as has been demonstrated for MODIS and VIIRS IR bands [63].

Considerable work is still needed to address the variability in solar illumination on the moon surface and the viewing geometry. This includes the development of an accurate model for infrared lunar radiance or approaches to remove the impact of different illumination and viewing geometry, and account for the partial saturation of the lunar images for IR bands.

VII. Conclusion

The configuration and feasibility of a notional U.S. GEO-HyIRS sensor and the architecture of its ground data processing system are discussed in this manuscript. Existing hyperspectral sounding instruments were reviewed to model a notional NOAA geostationary infrared sounder and to determine the ground segment system needs.

This article identifies and discusses some of the major technical challenges in the design and calibration of a

GEO-HyIRS sensor. Those results are expected to serve as references for the planning of the calibration, validation, and ground segment system of the U.S. GEO-HyIRS. The operational data processing system of the JPSS program was used as a reference for the generation of Level-1B and -2 proxy data. GEO-HyIRS Level-1B proxy data was generated using existing calibrated observations, in the form of SDR products, from the operational S-NPP and NOAA-20 CrIS sensors. A dedicated IR-only version of the operational NUCAPS retrieval system was developed to generate Level-2 proxy data. This includes profiles of thermodynamic and trace gas products. The generated GEO-HyIRS Level-2 thermodynamic products showed qualitative consistency with respect to operational NUCAPS IR-only Level-2 products and against the ECMWF model geophysical fields. Those results demonstrated the operability of key components of the GEO-HyIRS ground data processing system.

The usage of the PC compression technique to reduce the data volume of the GEO-HyIRS calibrated spectra was discussed. Compression ratios close to 10 are expected using this technique. The significant data volume reduction achieved with the application of PC compression justifies its usage to distribute the high temporal and spatial GEO-HyIRS calibrated observations. This approach is in line with the present plans for the distribution of the EUMETSAT IASI-NG and MTG-IRS calibrated spectra. Additional benefits of the application of PC compression include: 1) the reduction of random noise and 2) the possibility to better identify and remove artifacts in the calibrated spectra. A new approach dedicated to reduce the downlink data rate of the GEO-HyIRS observations was presented. This approach consists of the direct application of the PC compression to the measured GEO-HyIRS interferograms. The results show that this solution has the potential to further reduce the downlink data rate, while retaining most significant information content of the earth observations.

Since the GEO-HyIRS aims at higher spatial resolution than the current infrared sounders in LEO orbit, the quality of the geometric calibration becomes more critical. This is particularly important over heterogeneous regions, where geolocation errors could introduce large spatial representative errors, thus reducing the impact of the GEO-HyIRS observations. In this respect, the capabilities of lunar observations have been proposed to support the geometric as well as the radiometric calibration and validation of the GEO-HyIRS. It is recognized that significant work is still needed to improve the model for infrared lunar radiance; however, advances in the modeling of infrared lunar radiances are expected in the coming years.

Due to the large FPA size of the GEO-HyIRS, required to meet the temporal and spatial requirements, the correction of large spectral errors is expected. The methodologies to accurately correct those spectral errors to levels of a few parts per million exist and are well understood. The advantages and disadvantages between on-ground and on-board data processing were discussed. This helps us to identify the benefits of following the CrIS ground segment architecture for the design of the GEO-HyIRS ground segment system. In this regard, it is possible that the interferogram to spectra transformation, the nonlinearity correction and the spectral, radiometric, and geometric calibration can be performed as part of the on-ground data processing system.

In general, a successful NOAA geostationary infrared sounder program will benefit from the following:

1) the usage of standard and well-known procedures for the design of the ground segment system;
2) the application of mature calibration methodologies;
3) the lessons learned from the development and operation of existing and planned LEO/GEO infrared sounders;
4) the feedback from end-users.

In addition to that, new strategies and methodologies need to be explored and developed to overcome calibration and validation challenges of the GEO-HyIRS sensor. All the abovementioned along with a robust sensor design and a comprehensive on-ground and on-orbit sensor characterization will contribute to the generation of high quality GEO-HyIRS calibrated observations.

The operation of a U.S. GEO-HyIRS is critical to support and enhance Earth observational capabilities needed for numerical weather forecasting and environmental monitoring. The deployment of a U.S. GEO-HyIRS is expected to provide unique infrared hyperspectral measurements, with high temporal and spatial resolution over the Western Hemisphere, representing one of the future backbone observations of the global observing system. In this respect, the U.S. GEO-HyIRS will contribute to the next generation of earth observations from geostationary orbits and support the development of the geostationary ring of meteorological satellites. Observations from GEO-HyIRS are expected to contribute to satisfy present and future satellite needs and to be the foundation of new applications with significant societal, economic, and scientific benefits.

ACKNOWLEDGMENT

The authors would like to thank the support provided by Mr. K. L. Pryor, the NUCAPS science team lead. The scientific results and conclusions, as well as any views or opinions expressed herein, are those of the author(s) and do not necessarily reflect those of NOAA or the Department of Commerce.

REFERENCES

[1] M. T. Chahine *et al.*, "AIRS: Improving weather forecasting and providing new data on greenhouse gases," *Bull. Amer. Meteorol. Soc.*, vol. 87, pp. 911–926, 2006. [Online]. Available: https://doi.org/10.1175/BAMS-87-7-911

[2] F. Hilton *et al.*, "Hyperspectral earth observation from IASI: Five years of accomplishments," *Bull. Amer. Meteorol. Soc.*, vol. 93, pp. 347–370, 2012, doi: 10.1175/bams-d-11-00027.1.

[3] Y. Han *et al.*, "Suomi NPP CrIS measurements, sensor data record algorithm, calibration and validation activities, and record data quality," *J. Geophys. Res., Atmos.*, vol. 118, no. 22, pp. 12734–12748, Nov. 2013.

[4] Z. Li *et al.*, "Value-added impact of geostationary hyperspectral infrared sounders on local severe storm forecasts—via a quick regional OSSE," *Adv. Atmospheric Sci.*, vol. 3510, no. 10, pp. 1217–1230, 2018.

[5] J. Li *et al.*, "Warning information in a preconvection environment from the geostationary advanced infrared sounding system – A simulation study using IHOP case," *J. Appl. Meteorol. Climatol.*, vol. 50, pp. 776–783, 2011.

[6] K. Okamoto *et al.*, "Assessment of the potential impact of a hyperspectral infrared sounder on the himawari follow-on geostationary satellite," *SOLA*, vol. 16, pp. 162–168, Sep. 2020.

[7] T. A. Jones, S. Koch, and Z. Li, "Assimilating synthetic hyperspectral sounder temperature and humidity retrievals to improve severe weather forecasts," *Atmospheric Res.*, vol. 186, pp. 9–25, 2017. [Online]. Available: https://doi.org/10.1016/j.atmosres.2016.11.004

[8] S. Guedj, V. Guidard, B. Ménétrier, J.-F. Mahfouf, and F. Rabier, "Future benefits of high-density radiance data from MTG-IRS in the AROME fine-scale forecast model final report," [Research Report] Météo-France & CNRS/CNRM-GAME, Toulouse, France, Nov. 24, 2014. [Online]. Available: https://hal-meteofrance.archives-ouvertes.fr/meteo-01133380

[9] Q. Lu, C. Wu, C. Qi, X. Feng, H. Liu, and X. Xiao, "Brief introduction of the hyper-spectral infrared sounder from FY-4A and FY-3D," presented at the ECMWF Workshop Assimilation Hyper-spectral Geostationary Satell. Observ., Reading, UK, May 2017. [Online]. Available: https://www.ecmwf.int/node/17228

[10] C. Qi, C. Wu, L. Lee, Z. Ni, X. Hu, and L. Yang, "Latest status of HIRAS onboard FY-3D/3E and FY-4B/GIIRS," presented at the 23rd Int. TOVS Study Conf., Adv. Sounder Working Group Meeting, Virtual Meeting, Jun. 2021. [Online]. Available: https://cimss.ssec.wisc.edu/itwg/itsc/itsc23/working_groups/3%20202106-ASWG-Chengli%20Qi.pdf

[11] R. Yin *et al.*, "Impact of high temporal resolution FY-4A geostationary interferometric infrared sounder (GIIRS) radiance measurements on Typhoon forecasts: Maria (2018) case with GRAPES global 4D-var assimilation system," *Geophysical Res. Lett.*, vol. 48, pp. 1–10, 2021. [Online]. Available: https://doi.org/10.1029/2021GL093672

[12] Z. Ma *et al.*, "Four-dimensional wind fields from geostationary hyperspectral infrared sounder radiance measurements with high temporal resolution," *Geophysical Res. Lett.*, vol. 48, pp. 1–13, 2021. [Online]. Available: https://doi.org/10.1029/2021GL093794

[13] R. Yin *et al.*, "The evaluation of FY4A's geostationary interferometric infrared sounder (GIIRS) long-wave temperature sounding channels using the GRAPES global 4D-Var," *Quart. J. Roy. Meteorological Soc.*, vol. 146, no. 728, pp. 1459–1476, 2021.[Online]. Available: https://doi.org/10.1002/qj.3746.

[14] Meteosat Third Generation. Accessed: Jan. 20, 2022. [Online]. Available: https://earth.esa.int/web/eoportal/satellite-missions/m/meteosat-third-generation

[15] D. Coppens and B. Theodore, "MTG-IRS processing overview and performances," presented at the 21st Int. TOVS Study Conf., Darmstadt, Germany, 2017. Accessed: Jan. 20, 2022. [Online]. Available: http://library.ssec.wisc.edu/research_Resources/publications/pdfs/ITSC21/coppens01_ITSC21_2017.pdf

[16] D. Coppens and B. Theodore, "Spectral and radiometric characteristics of MTG-IRS," presented at the ECMWF Workshop Assimilation Hyperspectral Geostationary Satell. Observ., Reading, U.K., May 2017. [Online]. Available: https://www.ecmwf.int/node/17229

[17] K. Holmlund *et al.*, "Meteosat third generation (MTG): Continuation and innovation of observations from geostationary orbit," *Bull. Amer. Meteor. Soc.*, vol. 102, pp. E990–E1015, 2021.

[18] H. Wang, X. Huang, and Y. Chen, "An observing system simulation experiment for the impact of MTG candidate infrared sounding mission on regional forecasts: System development and preliminary results," *ISRN Meteorol.*, vol. 2013, pp. 1–18, 2013. [Online]. Available: http://dx.doi.org/10.1155/2013/971501

[19] T. J. Schmit *et al.*, "Validation and use of GOES sounder moisture information," *Weather Forecasting*, vol. 17, no. 1, pp. 139–154, Feb. 2002.

[20] T. J. Schmit *et al.*, "The GOES-R advanced baseline imager and the continuation of current sounder products," *J. Appl. Meteorol. Climatol.*, vol. 47, no. 10, pp. 2696–2711, 2008.

[21] Geostationary Extended Observations (GeoXO). Accessed: Jan. 20, 2022. [Online]. Available: https://www.nesdis.noaa.gov/next-generation-satellites/geostationary-extended-observations-geoxo

[22] World Meteorological Organization, "Vision for the WMO integrated global observing system in 2040," World Meteorological Organization, WMO-No. 124, Geneva, Switzerland, 2019. [Online]. Available: https://library.wmo.int/doc_num.php?explnum_id=10278

[23] Coordination Group for Meteorological Satellites, "CGMS high level priority plan (HLPP)," 2020–2024, no. 10, Darmstadt, Germany, Sep. 11, 2020. [Online]. Available: https://www.cgms-info.org/documents/CGMS_HIGH_LEVEL_PRIORITY_PLAN.pdf

[24] P. Menzel *et al.*, "Satellite-based atmospheric infrared sounder development and applications," *Bull. Amer. Meteor. Soc.*, vol. 99, no. 3, pp. 583–603, 2018.

[25] W. L. Smith, G. E. Bingham, and H. E. Revercomb, "GIFTS: Revolutionary observations for weather, chemistry, and climate applications," in *Optical Payloads for Space Missions*, Ch. 22. New York, NY, USA: Wiley, 2015. [Online]. Available: https://doi.org/10.1002/9781118945179.ch22

[26] M. Filonchyk, V. Hurynovich, H. Yan, A. Gusev, and N. Shpilevskaya, "Impact assessment of COVID-19 on variations of SO_2, No_2, CO and AOD over East China," *Aerosol Air Qual. Res.*, vol. 20, pp. 1530–1540, 2020, doi: 10.4209/aaqr.2020.05.0226.

[27] C. Clerbaux *et al.*, "Tracking pollutants from space: Eight years of IASI satellite observation," *Comptes Rendus Geosci.*, vol. 347, no. 3, pp. 134–144, 2015. [Online]. Available: https://doi.org/10.1016/j.crte.2015.06.001

[28] N. R. Nalli *et al.*, "Validation of carbon trace gas profile retrievals from the NOAA-unique combined atmospheric processing system for the cross-track infrared sounder," *Remote Sens.*, vol. 12, no. 19, Oct. 2020, Art. no. 3245.

[29] T. J. Schmit *et al.*, "High-spectral-and high-temporal-resolution infrared measurements from geostationary orbit," *J. Atmos. Ocean. Technol.*, vol. 26, pp. 2273–2292, 2009. [Online]. Available: https://journals.ametsoc.org/doi/10.1175/2009JTECHA1248.1

[30] H. Lin *et al.*, "Radiance preprocessing for assimilation in the hourly updating rapid refresh mesoscale model: A study using AIRS data. wea. forecasting," *Weather Forecasting*, vol. 32, pp. 1781–1800, Oct. 2017. [Online]. Available: https://doi.org/10.1175/WAF-D-17-0028.1

[31] F. Iturbide-Sanchez, S. R. S. da Silva, Q. Liu, K. L. Pryor, M. E. Pettey, and N. R. Nalli, "Toward the operational weather forecasting application of atmospheric stability products derived from NUCAPS CrIS/ATMS soundings," *IEEE Trans. Geosci. Remote Sens.*, vol. 56, no. 8, pp. 4522–4545, Aug. 2018, doi: 10.1109/TGRS.2018.2824829.

[32] L. Wang, Y. Chen, and Y. Han, "Impacts of field of view configuration of cross-track infrared sounder on clear-sky observations," *Appl. Opt.*, vol. 55, no. 25, pp. 7113–7119, Sep. 1, 2016, doi: 10.1364/AO.55.007113.

[33] W. Han, R. Knuteson, J. Li, D. Dee, and T. Auligne, "Assimilation of geostationary hyperspectral infrared sounders (GeoHIS): Opportunities and challenges," *JSCDA Quart. Newslett.*, no. 69, pp. 1–11, 2021. Accessed: Jan. 20, 2022. [Online]. Available: https://mcgovern-fagg.org/amy_html/pubs/JCSDA_Spring_69_4.30.21.pdf

[34] Private communication, Aug. 2021.

[35] T. J. Schmit *et al.*, "A closer look at the ABI on the GOES-R series," *Bull. Amer. Meteorol. Soc.*, vol. 98, pp. 681–698, 2017.

[36] S. Kalluri *et al.*, "From photons to pixels: Processing data from the advanced baseline imager," *Remote Sens.*, vol. 10, no. 2, pp. 1–28, 2018, doi: 10.3390/rs10020177.

[37] "Joint polar satellite system (JPSS) cross track infrared sounder (CrIS) sensor data records (SDR) algorithm theoretical basis document (ATBD) for full spectral resolution," [Online]. Available: https://www.star.nesdis.noaa.gov/jpss/documents/ATBD/D0001-M01-S01-002_JPSS_ATBD_CRIS-SDR_fsr_20180614.pdf

[38] Y. Chen, D. Tremblay, L. Wang, and F. Iturbide-Sanchez, "Improved lunar intrusion detection algorithm for the CrIS sensor data record," *IEEE Trans. Geosci. Remote Sens.*, vol. 58, no. 2, pp. 1134–1145, Feb. 2020.

[39] L. L. Strow *et al.*, "Spectral calibration and validation of the Cross-track infrared sounder on the Suomi-NPP satellite," *J. Geophysical Res.-Atmos.*, vol. 118, pp. 12486–12496, Nov. 2013.

[40] Y. Chen, Y. Han, and F. Weng, "Characterization of long-term stability of suomi NPP cross-track infrared sounder spectral calibration," *IEEE Trans. Geosci. Remote Sens.*, vol. 55, no. 2, pp. 1147–1159, Feb. 2017.

[41] Q. Liu *et al.*, "Community radiative transfer model for radiance assimilation and applications," in *Proc. IEEE Int. Geosci. Remote Sens. Symp.*, 2012, pp. 3700–3703, doi: 10.1109/IGARSS.2012.6350612.

[42] Y. Han *et al.*, "JCSDA Community radiative transfer model (CRTM) - Version 1," NOAA NESDIS, Silver Spring, MD, USA, NOAA Technical Report NESDIS 122, Aug. 2006. Accessed: Jan. 20, 2022. [Online]. Available: https://repository.library.noaa.gov/view/noaa/1157

[43] J. Susskind, C. D. Barnet, and J. M. Blaisdell, "Retrieval of atmospheric and surface parameters from airs/AMSU/HSB data in the presence of clouds," *IEEE Trans. Geosci. Remote Sens.*, vol. 41, no. 2, pp. 390–409, Feb. 2003.

[44] M. Goldberg, Y. Qu, L. M. McMillin, W. Wolf, L. Zhou, and M. Divakarla, "AIRS near-real-time products and algorithms in support of operational numerical weather prediction," *IEEE Trans. Geosci. Remote Sens.*, vol. 41, no. 2, pp. 379–389, Feb. 2003.

[45] C. Barnet *et al.*, "The NOAA unique combined atmospheric processing system (NUCAPS) algorithm theoretical basis document," Accessed: Apr. 21, 2021. [Online]. Available: https://www.star.nesdis.noaa.gov/jpss/documents/ATBD/ATBD_NUCAPS_v3.1.pdf

[46] L. L. Strow, S. E. Hannon, S. De Souza-Machado, H. E. Motteler, and D. Tobin, "An overview of the airs radiative transfer model," *IEEE Trans. Geosci. Remote Sens.*, vol. 41, no. 2, pp. 303–313, Feb. 2003.

[47] N. R. Nalli *et al.*, "Validation of atmospheric profile retrievals from the SNPP NOAA-unique combined atmospheric processing system. Part 2: Ozone," *IEEE Trans. Geosci. Remote Sens.*, vol. 56, no. 1, pp. 598–607, Jan. 2018.
[48] N. R. Nalli *et al.*, "Validation of atmospheric profile retrievals from the SNPP NOAA-Unique combined atmospheric processing system. Part 1: Temperature and moisture," *IEEE Trans. Geosci. Remote Sens.*, vol. 56, no. 1, pp. 180–190, Jan. 2018.
[49] N. R. Nalli *et al.*, "Validation of carbon trace gas profile retrievals from the NOAA-Unique combined atmospheric processing system for the cross-track infrared sounder," *Remote Sens.*, vol. 12, no. 19, 2020, Art. no. 3245, doi: 10.3390/rs12193245.
[50] NUCAPS product validated maturity reviews. [Online]. Available: https://www.star.nesdis.noaa.gov/jpss/documents/AMM/N20/NUCAPS_CO2_Validated.pdf
[51] B. Tournier, D. Blumstein, and F. Cayla, "IASI level 0 and 1 processing algorithm description," presented at the 12th Int. TOVS Study Conf. (ITSC-XII), Lorne, Victoria, Australia, 2002. Accessed: Jan. 20, 2022. [Online]. Available: https://cimss.ssec.wisc.edu/itwg/itsc/itsc12/presentations/6d5_B.Tournier.ppt
[52] D. C. Tobin, H. E. Revercomb, and R. O. Knuteson, "On-orbit spectral calibration of the geosynchronous imaging fourier transform spectrometer (GIFTS)," presented at the Characterizat. Radiomet. Calibrat. Remote Sens. Annu. Meeting (CALCON), Logan, Utah, USA, Sep. 2003.
[53] B. Huang *et al.*, "Lossless compression of three-dimensional hyperspectral sounder data using context-based adaptive lossless image codec with bias-adjusted reordering," *Opt. Eng.*, vol. 43, no. 9, pp. 2071–2079, 2004.
[54] EUMETSAT, "EPS product validation report: IASI L1 PCC PPF," EUM/OPS-EPS/REP/10/0148, v2, Aug. 2010. [Online]. Available: https://www-cdn.eumetsat.int/files/2020-04/pdf_iasi_l1_pcc_ppf.pdf
[55] H.-L. Huang and P. Antonelli, "Application of principal component analysis to high-resolution infrared measurement compression and retrieval," *J. Appl. Meteorol.*, vol. 40, pp. 365–388, 2000.
[56] S. Valle, W. Li, and S. J. Qin, "Selection of the number of principal components: The variance of the reconstruction error criterion with a comparison to other methods," *Ind. Eng. Chem. Res.*, vol. 38, pp. 4389–4401, 1999.
[57] P. Antonelli *et al.*, "A principal component noise filter for high spectral resolution infrared measurements," *J. Geophysical. Res. Atmos.*, vol. 109, Art. no. D23102, 2004, doi: 10.1029/2004JD004862.
[58] P. Wang, J. Li, and T. J. Schmit, "The impact of low latency satellite sounder observations on local severe storm forecasts in regional NWP," *Sensors*, vol. 20, p. 650, 2020. [Online]. Available: https://doi.org/10.3390/s20030650
[59] J. Garcıa-Sobrino, J. Serra-Sagrista, and J. Bartrina-Rapesta, "Hyperspectral IASI L1C data compression," *Sensors*, vol. 17, no. 6, Jun. 2017, Art. no. 1404.
[60] V. Zavyalov *et al.*, "Noise performance of the CrIS instrument," *J. Geophysical Res., Atmos.*, vol. 118, pp. 13108–13120, 2000.
[61] Z. Wang *et al.*, "On-orbit characterization of MODIS modulation transfer function using the Moon," *Trans. Geosci. Remote Sens.*, vol. 52, no. 7, pp. 4112–4121, 2014.
[62] L. Le Barbier *et al.*, "Moon study for IASI instruments inter-comparisons and absolute calibration," presented at the 3rd Joint GSICS/IVOS Lunar Calibrat. Works., Virtual, Nov. 2020.
[63] Z. Wang *et al.*, "Using the moon to evaluate the radiometric calibration performance of S-NPP VIIRS thermal emissive bands," *Proc. SPIE*, vol. 9218, 2016, Art. no. 92181W.

Flavio Iturbide-Sanchez (SeniorMember, IEEE) received the B.S.E.E degree in electronics engineering from Autonomous Metropolitan University, Mexico City, Mexico, in 1999, the M.S.E.E. degree in electrical engineering from the Advanced Studies and Research Center, National Polytechnic Institute, Mexico City, in 2001, and the Ph.D. degree in electrical and computer engineering from the University of Massachusetts, Amherst, MA, USA, in 2007.

His Ph.D. research focused on the miniaturization, development, calibration, and performance assessment of low-cost and power-efficient microwave radiometers for remote sensing applications. From 2001 to 2005, he was a Research Assistant with the Microwave Remote Sensing Laboratory, University of Massachusetts, where he was involved in the design, development, and characterization of highly integrated multichip modules and microwave circuits for low-noise, low-power consumption, high-gain, and high-stability microwave radiometers. From 2005 to 2007, he was with the Microwave Systems Laboratory, Colorado State University, Fort Collins, CO, USA, focusing on the demonstration of a low-cost and power-efficient compact microwave radiometer for humidity profiling. From 2008 to 2018, he supported the development of operational physical retrieval systems that employ hyperspectral-infrared and microwave observations implemented for the Polar Operational Environmental Satellites Project and the Joint Polar Satellite System. Since 2008, he has been a Physical Scientist with NOAA/NESDIS/Center for Satellite Applications and Research, College Park, MD, USA, where he has led the calibration and validation of the JPSS Cross-track Infrared Sounder instruments and supports the planning of the next generation of NOAA infrared and microwave sounders. His research interests include satellite remote sensing, satellite data assimilation, inverse theory applied to geoscience fields, weather forecasting, earth system science, small satellites, and the design of radiometer systems for earth observations based on emerging technologies.

Zhipeng Wang received the B.S. and M.S. degrees in optoelectronics from Tsinghua University, Beijing, China, in 2000 and 2003, respectively, and the Ph.D. degree in optics from the University of Arizona, Tucson, AZ, USA, in 2008.

He is currently a Principal Research Scientist with Science Systems and Applications Inc., Greenbelt, MD and a Member of NASA/GSFC Independent Calibration Team for CLARREO Pathfinder.

Satya Kalluri received the M.Sc. degree in geography from Osmania University, Hyderabad, India, in 1990 and the Ph.D. degree in geography from the University of Maryland College Park, College Park, MD, USA, in 1994.

He is currently the Program Scientist for the JPSS and LEO Program at NOAA NESDIS, College Park, MD, USA, and provides independent advice to the Program Director on sensor science and applications as well as overseeing the proving ground and risk reduction activities. He has more than 25 years of experience in the formulation, management, and development of several remote sensing missions. Prior to joining JPSS, he was a Division Chief with the NESIDS Center for Satellite Applications and Research (STAR). While working at STAR, he saw the development of algorithms and products to process remote sensing data from a variety of LEO and GEO satellite missions for NOAA and non-NOAA users in land and atmosphere applications. He led the development of the product generation and distribution segment of the GOES-R ground system with NOAA. Before joining NOAA, he was with the Aerospace Corporation, Raytheon and the University of Maryland at College Park on several remote sensing projects. His main research interests include land and atmosphere remote sensing.

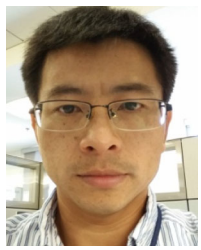

Yong Chen received the B.S. and M.S. degrees from Peking University, Beijing, China, in 1996 and 1999, respectively, and the Ph.D. degree from the University of California, Los Angeles, Los Angeles, CA, USA, in 2005, all in atmospheric sciences.

He is currently a Physical Scientist with NOAA/NESDIS/Center for Satellite Applications and Research, College Park, MD, USA. His research interests include radiative transfer theory and applications; development and implementation of fast radiative transfer model for satellite data assimilation; radiometric and spectral calibration and validation of satellite hyperspectral infrared sounders, IR data process; and global navigation satellite system radio occultation data processing and data assimilation.

Erin Lynch received the B.S. degrees in physics and mathematics, and the M.S. and Ph.D. degrees in atmospheric and oceanic science from the University of Maryland, College Park, MD, USA, in 2006, 2010, and 2017, respectively.

From 2019 to 2020, she was a Postdoctoral Research Associate with the Cooperative Institute for Satellite Earth System Studies/Earth System Science Interdisciplinary Center, University of Maryland, College Park, MD, USA. In 2021, she was a Remote Sensing Scientist with Global Science and Technology, Inc., Greenbelt, MD, USA supporting the CrIS SDR Team with NOAA/NESDIS/Center for Satellite Applications and Research providing postlaunch monitoring and assessment of the geometric calibration of the CrIS sensors and intercalibration with other hyperspectral infrared sounders. She is currently a Physical Scientist with NOAA/NESDIS/Office of Projects, Planning, and Analysis in Silver Spring, MD, USA where she develops concepts and plans for space weather satellite systems and sensors and conducts preformulation studies.

Murty Divakarla received the M.S. degree in meteorology and the Ph.D. degree in environmental monitoring from the University of Wisconsin-Madison, Madison, WI, USA, in 1990 and 1997, respectively.

He worked for a long time on the development of hyperspectral sounding retrieval algorithms and validations. He has been a contractor at the Center for Satellite Research and Applications (STAR), NOAA/NESDIS for the last 25 years and currently leads the NUCAPS Team at STAR as the Technical/Science Lead from IM Systems Group. He has numerous presentations in domestic and international conferences, and many publications in highly reputed journals.

Changyi Tan received the B.S. degree in astronomy from Nanjing University, Nanjing, China, in 2001, the M.S. degree in plasma physics from the Institute of Applied Physics and Computational Mathematics, Beijing, China, in 2004, and the Ph.D. degree in applied physics from the New Jersey Institute of Technology, Newark, NJ, USA, in 2010.

He is currently a Support Scientist with the I.M. Systems Group, College Park, MD, USA, where he performs research onsite at the NOAA/NESDIS Center for Satellite Applications and Research in support of JPSS NUCAPS algorithm development.

Tong Zhu received the B.S. degree in synoptic dynamics from the Nanjing Institute of Meteorology, Nanjing, China, the M.S. degree in atmospheric science from the Chinese Academy of Meteorological Sciences, Beijing, China, in 1988 and 1991, respectively, and the Ph.D. degree in atmospheric science from the University of Maryland, College Park, MD, USA, in 2003.

After graduation, he was with NOAA/NESDIS/STAR, first with CIRA/CSU for 15 years and then joined I.M. Systems Group, Inc., in 2019. His research interests include satellite remote sensing, including retrieval algorithm development, radiative transfer modeling, and satellite data application in numerical weather prediction and data assimilation.

Changyong Cao received the B.S. degree in geography from Peking University, Beijing, China, 1982, and the Ph.D. degree in geography specializing in remote sensing and geographic information systems from Louisiana State University, Baton Rouge, LA, USA, in 1992.

He is currently a Supervisory Research Physical Scientist, and the Chief for the Satellite Calibration and Data Assimilation Branch, NOAA Center for Satellite Applications and Research (STAR/SMCD). He specializes in the calibration of radiometers onboard NOAA's Operational Environmental Satellites, and currently leads the STAR radiance science, as well as the VIIRS sensor science teams. He is well known for his work on intersatellite calibration using the Simultaneous Nadir Overpass Method, which has become one of the cornerstones for the World Meteorological Organization Global Space-Based Inter-Calibration System. Before he joined NOAA, he was a Senior Scientist with five years of industry experience with a major aerospace company supporting NASA projects.

Dr. Cao was the recipient of three gold, one silver, and several bronze medals honored by the U.S. Department of Commerce and NOAA for his scientific and professional achievements. He was former Chair of the Committee on Earth Observation Satellites/Working Group on Calibration/Validation.